J. Fluid Mech. (2023), *vol*. 959, A27, doi:10.1017/jfm.2023.162

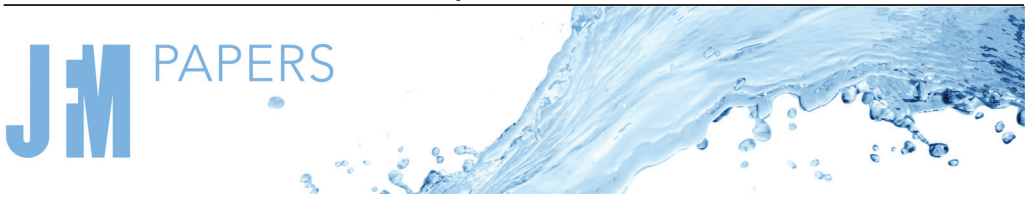

Shear-thickening suspensions down inclines: from Kapitza to Oobleck waves

Baptiste Darbois Texier[1,2], **Henri Lhuissier**[1], **Bloen Metzger**[1] and **Yoël Forterre**[1,†]

[1]Aix-Marseille University, CNRS, IUSTI, 13453 Marseille, France

[2]Université Paris-Saclay, CNRS, FAST, 91405 Orsay, France

(Received 23 September 2022; revised 7 January 2023; accepted 21 February 2023)

We investigate experimentally and theoretically the stability of a shear-thickening suspension flowing down an inclined plane. In a previous paper (Darbois Texier *et al.*, *Commun. Phys.*, vol. 3, 2020), we have shown that for particle volume fractions ϕ above the discontinuous shear-thickening fraction ϕ_{DST}, long surface waves grow spontaneously at a flow Reynolds number much below 1. This motivated a simplified analysis based on a purely inertialess mechanism, called the 'Oobleck waves' mechanism, which couples the negatively sloped rheology of the suspension with the free-surface deflection and captures well the experimental instability threshold and the wave speed, for $\phi > \phi_{DST}$. However, neglecting inertia does not allow us to describe the inertial Kapitza regime observed for $\phi < \phi_{DST}$, nor does it allow us to discriminate between Oobleck waves and other inertial instabilities expected above ϕ_{DST}. This paper fills this gap by extending our previous analysis, based on a depth-averaged approach and the Wyart–Cates constitutive shear-thickening rheology, to account for inertia. The extended analysis recovers quantitatively the experimental instability threshold in the Kapitza regime, below ϕ_{DST}, and in the Oobleck waves regime, above ϕ_{DST}. By providing additional measurements of the wave growth rate and investigating theoretically the effect of a strain delay in the rheology, it also confirms that the instability observed above ϕ_{DST} stems from the non-inertial Oobleck wave mechanism, which is specific to free-surface flows and dominates modes of inertial origin. These results emphasize the variety of instability mechanisms for shear-thickening suspensions and might be relevant to free-surface flows of other complex fluids displaying velocity-weakening rheology.

Key words: suspensions, thin films

† Email address for correspondence: yoel.forterre@univ-amu.fr.

1. Introduction

The resistance to flow of a shear-thickening suspension, such as an aqueous suspension of starch particles, increases steeply with increasing strain rate. Though it is no thicker than milk when it is stirred gently, the suspension may suddenly become rock-solid under high stresses or upon impact. This intriguing behaviour has been puzzling scientists for more than 80 years since the first study by Freundlich & Röder (1938). It is also an important question in industry (LaFarge 2013; Abdesselam *et al.* 2017; Blanco *et al.* 2019; Zarei & Aalaie 2020), where sudden thickening or jamming of the suspension can damage mixers or clog pipes, but it can also be harnessed to design new impact-resistant materials.

Shear-thickening arises when the suspension particles interact through a short-range repulsive force, which can stem from surface physical chemistry effects or Brownian motion. The repulsive force implies that the contacts between the particles transition from frictionless, under a small shear stress, to frictional, when the stress is large enough. This results in a large variation in the suspension viscosity at constant volume fraction, because the jamming volume fraction of the suspension depends on the frictional state between the particles (Guazzelli & Pouliquen 2018). This frictional transition scenario, first reported by Seto *et al.* (2013), has been supported by discrete numerical simulations (Mari *et al.* 2014; Dong & Trulsson 2017; Singh *et al.* 2018) and experiments performed at both contact and flow scales (Guy, Hermes & Poon 2015; Lin *et al.* 2015; Clavaud *et al.* 2017; Comtet *et al.* 2017; Hsu *et al.* 2018; Clavaud, Metzger & Forterre 2020). It has been rationalized by Wyart & Cates (2014) through a simple constitutive law assuming a stress-dependent jamming volume fraction, which reproduces successfully the different continuous shear-thickening (CST), discontinuous shear-thickening (DST) and shear-jamming (SJ) regimes observed experimentally (Guy *et al.* 2015, 2020; Mari *et al.* 2015*a*; Rathee, Blair & Urbach 2017; Morris 2018; Richards *et al.* 2019).

In particular, Wyart–Cates rheology and its later refinements (Singh *et al.* 2018; Richards *et al.* 2019; Ramaswamy *et al.* 2021) have a remarkable feature. Above a critical volume fraction, called ϕ_{DST}, the flow curve becomes S-shaped, with a negatively sloped region where the shear rate decreases with increasing stress. Such a non-monotonicity is known to promote unstable flow conditions (Yerushalmi, Katz & Shinnar 1970; Spenley, Yuan & Cates 1996; Olmsted 1999; Goddard 2003; Olmsted 2008; Nakanishi & Mitarai 2011; Divoux *et al.* 2016), and, indeed, shear-thickening suspension flows often destabilize and grow highly unsteady and inhomogeneous structures (Boersma *et al.* 1991; Lootens, Van Damme & Hébraud 2003; von Kann *et al.* 2011; Nagahiro, Nakanishi & Mitarai 2013; von Kann, Snoeijer & van der Meer 2013; Mari *et al.* 2015*b*; Hermes *et al.* 2016; Rathee *et al.* 2017; Chacko *et al.* 2018; Saint-Michel, Gibaud & Manneville 2018; Richards *et al.* 2019; Ovarlez *et al.* 2020; Sedes, Singh & Morris 2020; Gauthier *et al.* 2021). In most models, these instabilities are understood as an immediate consequence of the coupling between the S-shape rheology and inertia. Indeed, it can be shown that if the shear rate and shear stress are related instantaneously through a decreasing flow curve, then a simple shear flow is unstable along the flow direction only if inertia is taken into account (Spenley *et al.* 1996; Nakanishi & Mitarai 2011; Mari *et al.* 2015*b*).

Interestingly, we have reported recently an instability in the flow of a shear-thickening suspension down an inclined plane that does not rely on inertia (Darbois Texier *et al.* 2020). For a volume fraction above ϕ_{DST}, long surface waves grow spontaneously, in spite of a flow Reynolds number much smaller than 1. This instability was first observed by Balmforth, Bush & Craster (2005) but could not be modelled at the time due to the lack of appropriate flow rule for shear-thickening suspensions. We have proposed that these waves originate from the coupling between the free-surface deformation and the

negatively sloped rheology of the suspension, when the latter is forced into the DST region. The mechanism, which we coined the 'Oobleck waves' instability, is specific to surface flows and does not require inertia. It actually stems from the amplification of kinematic surface waves, by a mismatch between hydrostatics and the basal stress rheology. It has been supported by a depth-averaged analysis of the flow, neglecting inertia and using Wyart–Cates rheology, which has provided predictions in fair agreement with the instability threshold and wave speed measured above ϕ_{DST} (Darbois Texier *et al.* 2020).

However, this study leaves important open questions regarding the actual role of inertia on the formation of the surface waves. First, the non-inertial instability mechanism applies only for a volume fraction above ϕ_{DST}, when the flow curve is negatively sloped. Yet growing surface waves were also observed below ϕ_{DST}, where the flow curve is monotonic, though it was at a much larger Reynolds number than above ϕ_{DST} (Darbois Texier *et al.* 2020). These finite Reynolds number waves are certainly reminiscent of the Kapitza, or roll-waves, instability, which is observed for Newtonian (Jeffreys 1925; Kapitza & Kapitza 1948) and complex fluids, such as power-law fluids (Hwang *et al.* 1994; Ng & Mei 1994; Allouche *et al.* 2017), mud (Trowbridge 1987; Liu & Mei 1994; Balmforth & Liu 2004) and granular materials (Forterre & Pouliquen 2003; Forterre 2006). In all these cases, the Kapitza instability is inertia-driven and emerges above a critical Reynolds number (or Froude number), whose value depends on the precise rheology of the fluid. Therefore, inertia must be considered to obtain a complete description of the instability, including below ϕ_{DST}, and to understand the transition between the inertial Kapitza regime and the overdamped Oobleck wave regime. Addressing these questions represents a non-trivial test for the constitutive law of shear-thickening suspensions, which to date have been confronted primarily with steady rheological measurements.

A second issue about inertia, not addressed in our previous study, concerns its influence on the Oobleck wave instability itself, i.e. above ϕ_{DST}. A stability analysis neglecting inertia has proven sufficient to predict the correct behaviour for the instability threshold, suggesting that inertia is not involved in the instability mechanism. However, as mentioned above, even a small inertial component is known to give unstable modes for a negatively sloped flow curve, regardless of whether or not the flow has a free surface (Mari *et al.* 2015*b*). This raises an important fundamental question: Is the instability observed above ϕ_{DST} a purely non-inertial instability, resulting from the novel Oobleck wave mechanism specific to free-surface flows, or does it belong to the same class of inertial instabilities that have been reported so far for rheometric or confined shear-thickening flows (Richards *et al.* 2019)?

This paper addresses these questions by considering in details the role of inertia in the surface destabilization of a shear-thickening suspension flow down an incline. Section 2 details the experimental set-up, used already in Darbois Texier *et al.* (2020), and provides additional measurements of the instability growth rate, in both the dilute and concentrated regimes. Section 3 presents a linear stability analysis of the flow, using depth-averaged equations, assuming homogeneous volume fraction and accounting for hydrostatic contribution, Wyart–Cates rheology and the flow inertia. The predictions of the analysis are compared to the experimental observations in § 4. Finally, in § 5, the results and the competition between inertial and non-inertial modes are discussed in light of a refinement of the Wyart–Cates law introducing a strain delay in the rheology (Mari *et al.* 2015*b*; Chacko *et al.* 2018; Han *et al.* 2018; Richards *et al.* 2019). The conclusion (§ 6) confirms the novelty of the instability reported in the DST regime. Although inertial unstable modes also exist, the instability that actually emerges stems from the intrinsically non-inertial Oobleck mechanism, which is specific to free-surface flows.

2. Experiments

The same set-up as in Darbois Texier *et al.* (2020) was used to obtain complementary measurements of the instability growth rate, both below and above ϕ_{DST}. Below, we provide more details about the set-up and the different protocols used to characterize the instability onset in the two regimes.

2.1. *Shear-thickening suspension: composition and rheology*

We use an aqueous suspension of commercial organic cornstarch (Maisita®, www.agrana.com) prepared at a volume fraction ϕ, which is determined from the dry mass and density of the starch, $\rho_p = 1550\,\mathrm{kg\,m^{-3}}$. The starch particles (shown in figure 1*a*) are polydisperse angular grains, with average size approximately 15 µm. The rheology of the suspension was characterized in Darbois Texier *et al.* (2020) using a cylindrical Couette rheometer. The shear stress τ was imposed, and the shear rate $\dot{\gamma}$ was measured to obtain, for different volume fractions, the flow curves $\tau(\dot{\gamma})$, which are reproduced in figure 1(*b*). The measurements are fitted with the Wyart–Cates constitutive laws (Wyart & Cates 2014). The latter assume that the effective viscosity of the suspension diverges at a critical volume fraction ϕ_J, according to $\eta(\phi, f) = \eta_s(\phi_J(f) - \phi)^{-2}$, with η_s a prefactor proportional to the solvent viscosity. The jamming fraction itself depends on the fraction of frictional contacts f according to $\phi_J(f) = (1-f)\phi_0 + f\phi_1$, where ϕ_0 and ϕ_1 are the jamming fractions for a suspensions of frictionless and frictional particles, respectively. The fraction of frictional contacts is assumed to follow $f = \mathrm{e}^{-\tau^*/\tau}$, with τ^* the critical stress scale above which frictional contacts are activated. We follow the fitting procedure of Guy *et al.* (2015) to fit our measurements with the model, and obtain $\eta_s = 0.91 \pm 0.01$ mPa s, $\phi_0 = 0.52 \pm 0.005$, $\phi_1 = 0.43 \pm 0.005$ and $\tau^* = 12 \pm 2$ Pa. With these parameters, the Wyart–Cates model captures fairly well (i) the low-stress part (frictionless regime) of the rheogram for all ϕ, (ii) the CST part observed for moderate ϕ, and (iii) the onset of DST, i.e. the lowest stress at which the curve presents a negative slope ($\mathrm{d}\tau/\mathrm{d}\dot{\gamma} < 0$), for volume fractions above $\phi_{DST} \equiv \phi_0 - 2\mathrm{e}^{-1/2}(\phi_0 - \phi_1) \simeq 0.41$. Above the threshold stress of discontinuity, the flow inside the rheometer is highly unsteady and inhomogeneous (Guy *et al.* 2015; Saint-Michel *et al.* 2018; Richards *et al.* 2019; Ovarlez *et al.* 2020; Gauthier *et al.* 2021), and the experimental rheogram can no longer be fitted with the model rheology.

2.2. *Determination of the instability threshold*

2.2.1. *Experiments at low ϕ (Kapitza waves)*

Figure 1(*c*) shows a sketch of the experimental set-up used to characterize the stability threshold at low volume fractions ($\phi < \phi_{DST}$). The set-up consists of a 1 m long and 10 cm wide plane, which can be tilted at angle θ, varied between 2° and 22°. The inclined plane is covered with a diamond lapping film of typical roughness 45 µm to prevent wall-slip. The flow is controlled by the gravity-driven drainage of a reservoir of suspension through a gate located at the top of the plane. Two low-incidence laser sheets and two cameras are used to measure the mean film thickness $h_0 \sim 2$–10 mm, and the crest-to-crest amplitudes of the waves, Δh_1 and Δh_2, at distances $x_1 = 10$ cm and $x_2 = 70$ cm from the gate. The calibration of the laser incidence yields a precision in the local measurement of h_0, Δh_1 and Δh_2 of $\sim$10 µm. The current flow rate q of the suspension is measured with a scale placed at the bottom end of the incline. The current Reynolds number of the flow is computed from the current flow rate q and mean film thickness h_0, using the relation

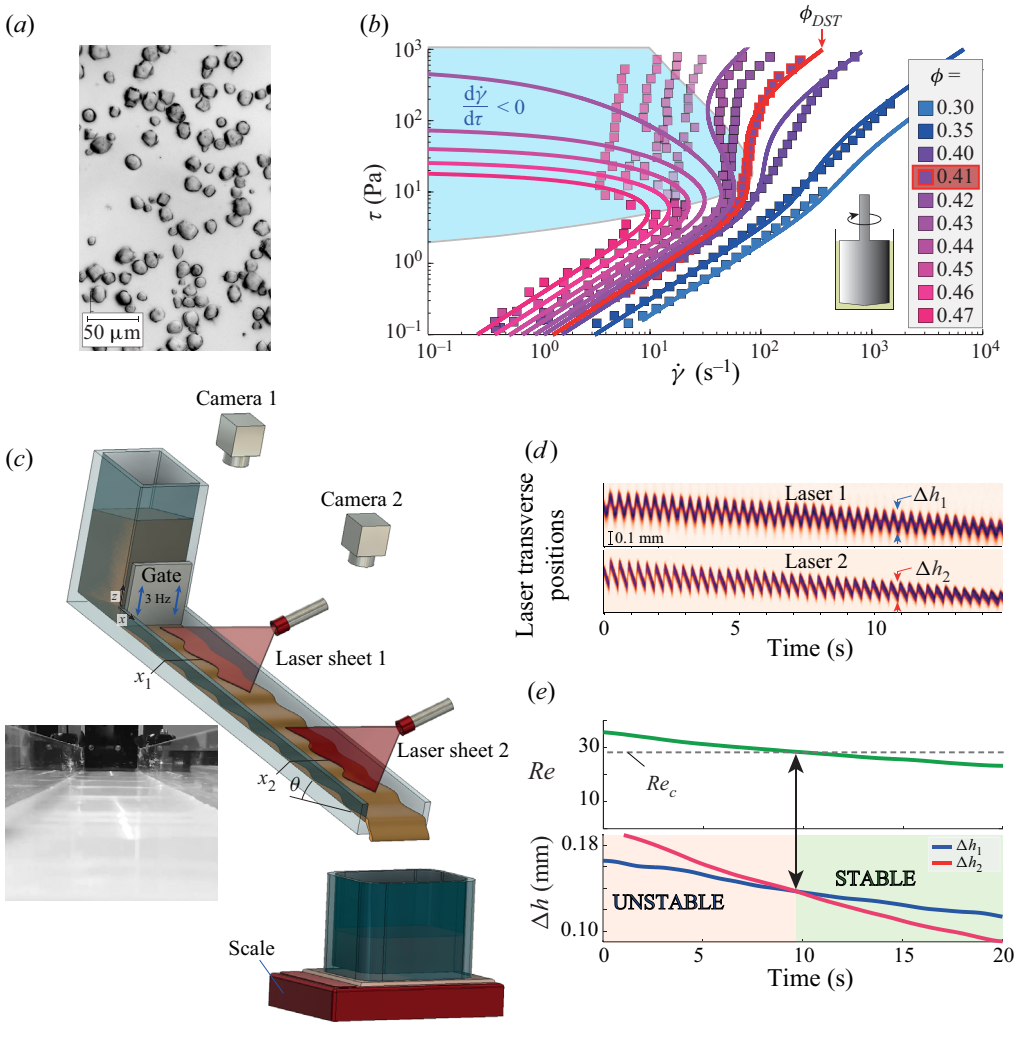

Figure 1. Rheograms and experiments at low ϕ to characterize the Kapitza instability. (*a*) Image of the cornstarch grains. (*b*) Rheograms of the aqueous cornstarch suspension for various volume fractions. Solid lines: Wyart–Cates rheology with $\eta_s = 0.91$ mPa s, $\phi_0 = 0.52$, $\phi_1 = 0.43$ and $\tau^* = 12$ Pa. The region where $d\tau/d\dot\gamma < 0$ is highlighted in blue. (*c*) Sketch of the set-up used to characterize the instability below ϕ_{DST}, and a typical picture of the Kapitza waves ($\phi = 0.33$, $\theta = 2^\circ$, $Re \simeq 37$). (*d*) Spatio-temporal plots showing the transverse displacement of the intersection between the laser sheet and the flow surface, at the top and at the bottom of the incline ($\phi = 0.33$, $\theta = 2^\circ$, $Re \simeq 37$). (*e*) Reynolds number of the flow, and amplitude of the perturbation at the top, Δh_1, and at the bottom, Δh_2, of the incline ($\phi = 0.36$, $\theta = 3^\circ$, $Re \simeq 28$). The black dashed line indicates the instability threshold Re_c. Plots (*d*,*e*) are reproduced from Darbois Texier *et al.* (2020).

$Re = 3q^2/(gh_0^3 \sin\theta)$, with g the gravitational acceleration. This definition, which does not depend explicitly on the suspension viscosity η, is convenient since it can be used whatever the rheology of the fluid. The factor 3 is chosen so as to recover $Re = \rho\,\bar u_0 h_0/\eta_0$, with $\bar u_0 = q/h_0$ the depth-averaged velocity, for a steady Newtonian flow (Landau & Lifshitz 2013).

To determine the instability threshold, a small perturbation is imposed on the flow, while the flow rate decreases quasi-steadily because of the slow drainage of the reservoir

(the variation is sufficiently slow to ensure a uniform flow rate along the incline). The perturbation is forced by modulating sinusoidally the aperture of the gate (at 3 Hz, with amplitude $\pm 100\,\mu$m), with the help of a translating stage. The perturbation is convected, and its amplification or damping is monitored by measuring the amplitude at x_1 and x_2 (see figure 1*d*).

Figure 1(*e*) shows a typical evolution of the Reynolds number Re, together with the wave amplitude at the top (x_1) and at the bottom (x_2) of the incline, starting from an unstable situation where $\Delta h_2 > \Delta h_1$. The instability threshold is determined from the current flow rate at the time $\Delta h_2 = \Delta h_1$, which sets the critical Reynolds number Re_c (dashed line in figure 1*e*), the critical flow thickness h_c, the critical mean flow velocity u_c, and the critical basal shear stress $\tau_c = \rho g h_c \sin\theta$.

2.2.2. *Experiments at high ϕ (Oobleck waves)*

For a volume fraction above ϕ_{DST}, the instability changes qualitatively. The perturbation is either dampened or amplified and saturated over a very short distance ($\sim$1 cm), which compares with the flow thickness, instead of increasing or decreasing gently all along the inclined plane, as for $\phi < \phi_{DST}$. Forcing the instability is no longer useful because the most unstable modes of the perturbative noise background dominate wave formation. Moreover, for $\phi > \phi_{DST}$, it is not possible to set the flow with the draining reservoir because the jamming of the suspension at the gate creates large perturbations, which prevent studying the stability over the incline. To circumvent these issues, a modified injection system is used above ϕ_{DST}. The suspension is discharged from a large funnel into an upper pool, which lets the discharge perturbations decay before feeding the incline by a gentle overflow (see figure 2*a*). To increase the suspension flow rate quasi-steadily, the funnel's aperture is opened slowly with the help of a translating stage. In this case, the wave amplitude grows over a short distance (see figure 2*b*), which allows characterizing the wave growth rate with a single laser sheet and camera. Figure 2(*c*) presents the simultaneous evolution of Re, Δh_1 and Δh_2, as obtained with this protocol, starting from a stable situation where $\Delta h_2 < \Delta h_1$. As previously, the stability threshold is reached when $\Delta h_2 = \Delta h_1$, providing Re_c, h_c, u_c and τ_c.

For both protocols (above and below ϕ_{DST}), we have verified that the same instability criteria are obtained from successive steady-state measurements at various constant flow rates. For each volume fraction investigated, experiments are repeated at least four times, and for each repetition, a new, freshly prepared, suspension is used to avoid starch aging or evaporation issues.

2.2.3. *Wave speed and growth rate measurements*

Besides the instability threshold, three important properties characterizing the surface wave propagation are extracted from these experiments. From the measured steady-state relation $q(h_0)$ between the average flow rate and the mean layer thickness, we obtain an experimental determination of the kinematic wave speed $c_{kin} = \mathrm{d}q/\mathrm{d}h_0$, which will turn out to be important to discriminate between the different instability mechanisms.

From the evolution of the amplitude and phase of the wave along the plane, we measure the growth rate and wave speed. It was not possible to obtain experimentally the complete dispersion relation as a function of the wave frequency, because for $\phi > \phi_{DST}$, the waves are most often dominated, within a very short distance, by the nonlinear growth of the most unstable mode of the background noise, regardless of the forcing frequency. Therefore, to characterize the strength of the instability, we focused the growth rate measurements on

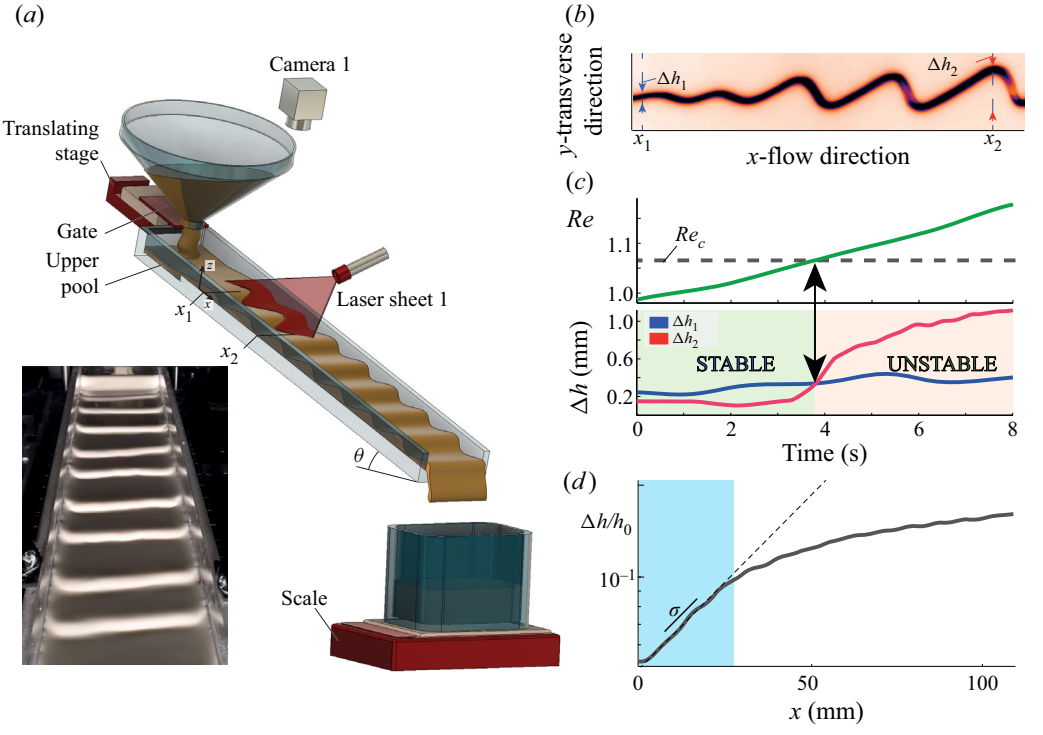

Figure 2. Experiments at high ϕ to characterize the Oobleck waves. (*a*) Sketch of the set-up used for $\phi > \phi_{DST}$, and a typical image of Oobleck waves ($\phi = 0.45, \theta = 10°, Re \simeq 1.14 \simeq 0.2\, Re_{Kap}$). (*b*) Image of the flow surface intersected by the laser sheet (same conditions as in *a*). (*c*) Reynolds number of the flow and amplitude of the perturbation Δh_1 and Δh_2 (same conditions as in *a*). The black dashed line indicates the instability threshold Re_c. (*d*) Normalized wave amplitude $\Delta h/h_0$ as a function of x (same ϕ and θ, $Re/Re_c = 1.05$). The growth rate is measured over the region highlighted in blue.

the most unstable mode just above the instability threshold, i.e. at an arbitrary distance above the threshold $(Re - Re_c)/Re_c = 0.05$. For low volume fractions $\phi < \phi_{DST}$, the wave grows exponentially all along the incline. The spatial growth rate σ is obtained from the amplitude measurements at x_1 and x_2, according to $\sigma = \ln(\Delta h_2/\Delta h_1)/(x_2 - x_1)$. For large volume fractions ($\phi > \phi_{DST}$), the amplitude of $\Delta h(x)/h_0$ saturates within a shorter distance, as shown in figures 2(*b*,*d*). In this case, the growth rate is measured by fitting the short initial exponential regime, which is highlighted in blue. In both cases, the reported wave speed is that of the most unstable mode.

3. Linear stability analysis

To rationalize the instability observed experimentally, we perform a linear stability analysis of the flow. The depth-averaged approach and the approximation of homogeneous volume fraction used in Darbois Texier *et al.* (2020) is extended to include inertial terms. This approach has the advantage of embedding the complex rheology of the suspension in a single term, the basal stress, while not limiting significantly the scope of the analysis, since the most unstable modes will turn out to be slender-sloped. The rheology of the shear-thickening suspension is modelled by the Wyart–Cates flow rule introduced in § 2.1.

3.1. *Base flow*

We compute, first, the base flow, i.e. the steady uniform flow of a shear-thickening suspension, with volume fraction ϕ, density ρ, and thickness h_0, down a plane with slope θ. The base state will be denoted by the subscript 0. For a layer with a stress-free surface, the momentum balance imposes that the shear stress τ_0 increases linearly with the depth $h_0 - z$, according to

$$\tau_0(z) = \rho g (h_0 - z) \sin\theta. \tag{3.1}$$

On the other hand, the shear stress is related to the shear rate by

$$\tau_0(z) = \eta(\phi, z)\, \frac{\mathrm{d}u_0(z)}{\mathrm{d}z}, \tag{3.2}$$

with $u_0(z)$ the suspension velocity parallel to the plane, and $\eta(\phi, z)$ the suspension viscosity, which is generally not uniform. Combining (3.1) with (3.2) yields the velocity profile in terms of the reduced variable τ_0:

$$u_0(\tau_0) = \frac{1}{\rho g \sin\theta} \int_{\tau_0}^{\tau_{b,0}} \frac{\tau'}{\eta(\phi, \tau')}\, \mathrm{d}\tau', \tag{3.3}$$

where $\tau_{b,0} \equiv \tau_0(z = 0) = \rho g h_0 \sin\theta$ is the basal shear stress. Finally, the viscosity is given by the Wyart–Cates expression

$$\eta(\phi, \tau) = \eta_s \left[\phi_0 \left(1 - \mathrm{e}^{-\tau^*/\tau}\right) + \phi_1\, \mathrm{e}^{-\tau^*/\tau} - \phi\right]^{-2}, \tag{3.4}$$

where η_s, τ^*, ϕ_0 and ϕ_1 are the rheological parameters introduced in § 2.1.

Figure 3 shows the base flow velocity profile obtained by integrating (3.3) numerically using (3.4), for volume fractions between 0.30 and 0.48. For low ϕ, the velocity profile is semi-parabolic, as expected for a Newtonian fluid. For increasing ϕ, the concavity of the profile reverses, which reflects the increase in the suspension viscosity at the bottom of the layer where the stress is the largest. The flowing region even localizes close to the free surface when the suspension jams beneath, i.e. when the basal stress reaches

$$\tau_{b,SJ} = \frac{\tau^*}{\ln\left(\dfrac{\phi_0 - \phi_1}{\phi_0 - \phi}\right)}. \tag{3.5}$$

Note that the vertical gradient of shear is expected to drive particle migration from the bottom to the top of the layer, which in turn should slightly modify the velocity profile (Carpen & Brady 2002; Dhas & Roy 2022). For simplicity, we do not consider this coupling between flow and volume fraction variation, which is not essential to account for the instabilities studied here.

In the following analysis, we will use depth-averaged quantities and restrict the calculations to $\tau_{b,0} < \tau_{b,SJ}$, which does not affect the flow stability prediction (see figures 7*b* and 9*c*). From (3.3), the depth-averaged velocity of the base flow, $\bar{u}_0 =$

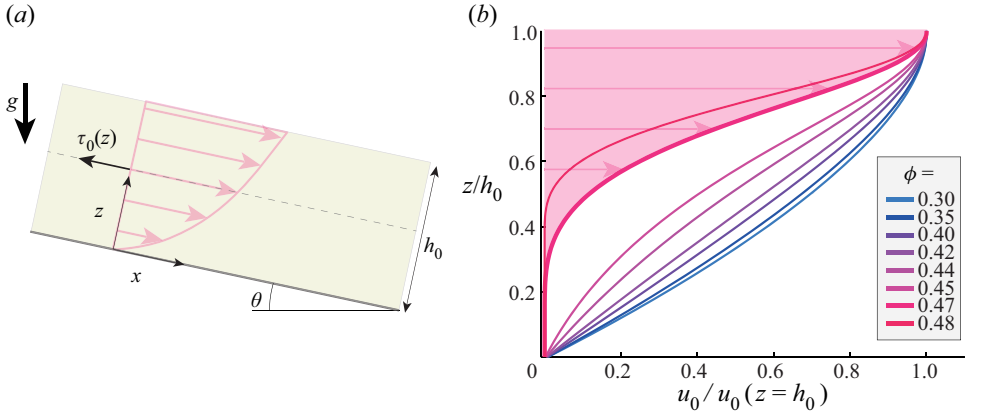

Figure 3. (*a*) Sketch of the notations. (*b*) Velocity profiles of the base flow for the Wyart–Cates rheology with the parameters obtained from figure 1(*b*) and for various volume fractions ($\tau_{b,0}/\tau^* = 2$).

$(1/h_0)\int_0^{h_0} u_0(z)\,\mathrm{d}z = (1/\tau_{b,0})\int_0^{\tau_{b,0}} u_0(\tau)\,\mathrm{d}\tau$, is given by

$$\bar{u}_0 = \frac{h_0}{\tau_{b,0}^2}\int_0^{\tau_{b,0}}\int_\tau^{\tau_{b,0}} \frac{\tau'}{\eta(\phi,\tau')}\,\mathrm{d}\tau'\,\mathrm{d}\tau. \tag{3.6}$$

This expression can be recast into a formal effective rheological law relating the basal stress $\tau_{b,0}$ to the effective shear rate $\bar{u}_0/h_0$, as

$$\frac{\bar{u}_0}{h_0} = \frac{\tau_{b,0}}{3\eta(\phi,\tau_{b,0})}\,\mathcal{G}(\phi,\tau_{b,0}), \tag{3.7}$$

where the function $\mathcal{G}$ is defined as

$$\mathcal{G}(\phi,\tau_b) = \frac{3\eta(\phi,\tau_b)}{\tau_b^3}\int_0^{\tau_b}\int_\tau^{\tau_b} \frac{\tau'}{\eta(\phi,\tau')}\,\mathrm{d}\tau'\,\mathrm{d}\tau. \tag{3.8}$$

For a Newtonian fluid with a uniform viscosity, $\mathcal{G} = 1$. One recovers the basal stress relation for a steady uniform Newtonian flow, $\tau_{b,0} = 3\eta\bar{u}_0/h_0$, where the factor 3 is a signature of the semi-parabolic velocity profile. For the Wyart–Cates shear-thickening law (3.4), $\mathcal{G}$ is no longer constant and depends on both the volume fraction ϕ and the relative basal stress $\tau_{b,0}/\tau^*$.

Finally, the Reynolds number of the base flow is given by

$$Re = \frac{3\bar{u}_0^2}{gh_0\sin\theta} = \frac{\tau_{b,0}^3\,\mathcal{G}(\phi,\tau_{b,0})^2}{3\,\eta(\phi,\tau_{b,0})^2\rho g^2\sin^2\theta}. \tag{3.9}$$

The latter depends on three of the four main dimensionless parameters of the problem, namely, the Reynolds number based on the suspending liquid viscosity, $Re_s = \tau_{b,0}^3/(3\eta_s^2\rho g^2\sin^2\theta)$, the volume fraction ϕ, and the magnitude of the basal shear stress relative to the repulsive stress, $\tau_{b,0}/\tau^*$, two of which are controlled by the flow thickness h_0. The fourth parameter is the inclination angle θ.

The base state flow rule (3.7)–(3.8) summarizes the rheological behaviour of the suspension flow. It will be used in the following to study stability.

3.2. *Depth-averaged equations*

To study flow stability, we take advantage of the long nature of the observed waves, whose wavelength ($\sim$10 cm) is much larger than the layer thickness ($h_0 \lesssim 1$ cm). In this long wave limit, the vertical momentum balance implies that the pressure distribution is hydrostatic to the lowest order, and that horizontal viscous stress gradients can be neglected. Integrating the mass and horizontal momentum equations across the flow, for an incompressible medium, yields the depth-averaged, or Saint-Venant, equations

$$\frac{\partial h}{\partial t} + \frac{\partial h\bar{u}}{\partial x} = 0, \tag{3.10}$$

$$\rho\left(\frac{\partial h\bar{u}}{\partial t} + \frac{\partial h\overline{u^2}}{\partial x}\right) = \rho g h \sin\theta - \tau_b - \rho g h \cos\theta \frac{\partial h}{\partial x}, \tag{3.11}$$

where $h(x,t)$ is the flow thickness, $\bar{u}(x,t) = (1/h)\int_0^h u(x,z,t)\,\mathrm{d}z$ is the depth-averaged velocity, $\overline{u^2} = (1/h)\int_0^h u^2(x,z,t)\,\mathrm{d}z$ is the averaged square velocity, and $u(x,z,t)$ is the parallel velocity component. The right-hand-side terms in (3.11) correspond to the gravity term, the basal shear stress, and the resultant of the horizontal gradient of hydrostatic pressure, respectively. To derive the last term, the normal stress tensor of the fluid is assumed isotropic at the lowest order.

To solve the system, closure relations are required for the basal stress τ_b and momentum flux term $\overline{u^2}$. Following a common approach in roll-wave studies (Kapitza & Kapitza 1948; Trowbridge 1987; Ng & Mei 1994; Forterre & Pouliquen 2003), we assume that the base state flow rule (3.7)–(3.8), derived for a steady uniform flow, remains valid for an unsteady, non-uniform flow in the long-wavelength limit, which implies

$$\frac{\bar{u}}{h} = \frac{\tau_b}{3\eta(\phi,\tau_b)}\,\mathcal{G}(\phi,\tau_b) \equiv \dot{\gamma}(\tau_b). \tag{3.12}$$

Similarly, we rewrite the momentum flux term as $\overline{u^2} = \alpha\bar{u}^2$, and assume that the factor α, which is set by the shape of the velocity profile, is constant and equal to the base state value. From (3.3), we obtain

$$\alpha = \frac{\tau_{b,0}\displaystyle\int_0^{\tau_{b,0}}\left(\int_\tau^{\tau_{b,0}}\frac{\tau'}{\eta(\phi,\tau')}\,\mathrm{d}\tau'\right)^2\mathrm{d}\tau}{\displaystyle\left(\int_0^{\tau_{b,0}}\int_\tau^{\tau_{b,0}}\frac{\tau'}{\eta(\phi,\tau')}\,\mathrm{d}\tau'\,\mathrm{d}\tau\right)^2}. \tag{3.13}$$

For a Newtonian fluid (uniform viscosity), $\alpha = 6/5$. This value increases as the flow localizes closer and closer beneath the surface. We will see that the instability threshold can be shifted significantly by the value of α at large volume fractions.

3.3. *Linearization*

To analyse the linear stability of the base state flow we non-dimensionalize equations using $\tilde{h} = h/h_0$, $\tilde{x} = x/h_0$, $\tilde{u} = \bar{u}/\bar{u}_0$, $\tilde{t} = t\,\bar{u}_0/h_0$, $\tilde{\tau}_b = \tau_b/\tau_{b,0}$ and $\tilde{\dot{\gamma}} = \dot{\gamma}h_0/\bar{u}_0$.

The conservation equations and flow rule (3.10)–(3.12) become

$$\frac{\partial \tilde{h}}{\partial \tilde{t}} + \frac{\partial \tilde{h}\tilde{u}}{\partial \tilde{x}} = 0, \tag{3.14}$$

$$\frac{Re}{3}\left(\frac{\partial \tilde{h}\tilde{u}}{\partial \tilde{t}} + \alpha \frac{\partial \tilde{h}\tilde{u}^2}{\partial \tilde{x}}\right) = \tilde{h} - \tilde{\tau}_b - \frac{\tilde{h}}{\tan\theta}\frac{\partial \tilde{h}}{\partial \tilde{x}}, \tag{3.15}$$

$$\frac{\tilde{u}}{\tilde{h}} = \tilde{\dot{\gamma}}(\tilde{\tau}_b), \tag{3.16}$$

where Re is given by (3.9).

Considering a small perturbation of the base flow, $\tilde{h} = 1 + h_1$, $\tilde{u} = 1 + u_1$, $\tilde{\tau}_b = 1 + \tau_1$, with $|h_1|, |u_1|, |\tau_1| \ll 1$, (3.14)–(3.16) become, at the lowest order,

$$\frac{\partial h_1}{\partial \tilde{t}} + \frac{\partial h_1}{\partial \tilde{x}} + \frac{\partial u_1}{\partial \tilde{x}} = 0, \tag{3.17}$$

$$\frac{Re}{3}\left(\frac{\partial u_1}{\partial \tilde{t}} + (\alpha - 1)\frac{\partial h_1}{\partial \tilde{x}} + (2\alpha - 1)\frac{\partial u_1}{\partial \tilde{x}}\right) = h_1 - \tau_1 - \frac{1}{\tan\theta}\frac{\partial h_1}{\partial \tilde{x}}, \tag{3.18}$$

$$u_1 - h_1 = A\tau_1, \tag{3.19}$$

where A is defined as

$$A \equiv \left(\frac{\mathrm{d}\tilde{\dot{\gamma}}}{\mathrm{d}\tilde{\tau}_b}\right)_{\tilde{\tau}_b=1} = \frac{\tau_{b,0}h_0}{\bar{u}_0}\left(\frac{\mathrm{d}\dot{\gamma}}{\mathrm{d}\tau_b}\right)_{\tau_b=\tau_{b,0}} = \frac{3}{\mathcal{G}(\phi, \tau_{b,0})} - 2, \tag{3.20}$$

and use has been made of the identity

$$\frac{\mathrm{d}}{\mathrm{d}\tau}\left(\int_0^\tau \int_{\tau'}^\tau \frac{\tau''}{\eta(\phi, \tau'')}\,\mathrm{d}\tau''\,\mathrm{d}\tau'\right) = \frac{\tau^2}{\eta(\phi, \tau)}. \tag{3.21}$$

The parameter A represents the dimensionless inverse slope of the flow rule between the effective shear rate $\tilde{u}/h$ and the basal stress $\tilde{\tau}_b$. For a shear-thickening suspension following the Wyart–Cates flow rule, A depends on ϕ and $\tau_{b,0}/\tau^*$. It is equal to 1 for a Newtonian flow, and is negative for DST.

Overall, the linearized system (3.17)–(3.19) involves four dimensionless parameters, θ, Re, α and A (which are alternatives to those listed above, namely θ, Re_s, $\tau_{b,0}/\tau^*$ and ϕ).

3.4. *Modes and stability diagram*

The system (3.17)–(3.19) is solved for a normal mode $h_1 = H\exp(\mathrm{i}(\tilde{k}\tilde{x} - \tilde{\omega}\tilde{t}))$, $u_1 = U\exp(\mathrm{i}(\tilde{k}\tilde{x} - \tilde{\omega}\tilde{t}))$, with dimensionless wavenumber $\tilde{k}$ and dimensionless pulsation $\tilde{\omega}$. A non-trivial solution exists only if

$$\det\begin{pmatrix} \mathrm{i}(\tilde{k} - \tilde{\omega}) & \mathrm{i}\tilde{k} \\ \dfrac{\mathrm{i}}{\tan\theta}\tilde{k} + \dfrac{Re}{3}(\alpha - 1)\mathrm{i}\tilde{k} - \left(1 + \dfrac{1}{A}\right) & \dfrac{Re}{3}(\mathrm{i}\tilde{k}(2\alpha - 1) - \mathrm{i}\tilde{\omega}) + \dfrac{1}{A} \end{pmatrix} = 0, \tag{3.22}$$

which provides the dispersion relation

$$-\frac{Re}{3}\tilde{\omega}^2 + \left(\frac{2\,Re}{3}\alpha\tilde{k} - \frac{\mathrm{i}}{A}\right)\tilde{\omega} + \left(\frac{1}{\tan\theta} - \frac{Re\,\alpha}{3}\right)\tilde{k}^2 + \left(1 + \frac{2}{A}\right)\mathrm{i}\tilde{k} = 0. \tag{3.23}$$

We conduct the temporal stability analysis with $\tilde{k}$ real and $\tilde{\omega}$ complex. Equation (3.23) is of order 2 in ω and has two branches. Each of these may actually embed different

instabilities depending on the point of the phase space considered. To get insight into the physical meaning and stability of the branches, it is instructive to study their behaviour at low $\tilde{k}$, before giving the exact solutions. The structure of the dispersion relation ensures that the growth rate $\tilde{\sigma} = \mathrm{Im}[\tilde{\omega}(\tilde{k})]$ is monotonic and does not change sign with $\tilde{k}$, which means that the stability criterion at low $\tilde{k}$ is valid for all wavenumbers. Expanding the pulsation as $\tilde{\omega} = ia_0 + c\tilde{k} + ia_2\tilde{k}^2$ in the dispersion relation (3.23) gives the following two solutions at the lowest order in $\tilde{k}$:

$$\tilde{\omega}_1 \simeq (2+A)\tilde{k} + \mathrm{i}A\left[\frac{Re}{3}\left[(2+A)(2+A-2\alpha)+\alpha\right] - \frac{1}{\tan\theta}\right]\tilde{k}^2, \tag{3.24}$$

$$\tilde{\omega}_2 \simeq (2\alpha - 2 - A)\tilde{k} - \mathrm{i}\,\frac{3}{A\,Re}. \tag{3.25}$$

The first branch, $\tilde{\omega}_1(\tilde{k})$, is the 'kinematic' branch, since its wave speed in the long wave limit ($\tilde{k} \to 0$), $\tilde{c}_1 = \mathrm{Re}(\tilde{\omega}_1)/\tilde{k} = 2 + A$, is that of kinematic waves, i.e. the slender small-amplitude waves that propagate at the speed $c_{kin} = (\mathrm{d}q/\mathrm{d}h)_0 = \bar{u}_0 + h_0(\mathrm{d}\bar{u}/\mathrm{d}h)_0$, obtained by combining the steady flow rule $\bar{u}(h)$ with the mass equation (3.10) (Whitham 2011). Indeed, c_{kin} can be expressed in terms of A by noting that $\bar{u}(h)$ satisfies the force balance $\tau_b[\bar{u}(h)/h] = \rho g h \sin\theta$, in the base state. Differentiating with respect to h and making use of the definition of A in (3.20), one recovers $\tilde{c}_{kin} = 1 + (h_0/\bar{u}_0)(\mathrm{d}\bar{u}/\mathrm{d}h)_0 = 2 + A$.

The kinematic branch $\tilde{\omega}_1(\tilde{k})$ is unstable when the growth rate $\tilde{\sigma}_1 \equiv \mathrm{Im}(\tilde{\omega}_1)$ is positive. Depending on the sign of A, two cases must be considered, which will be shown to concern two different instabilities. For $A > 0$, i.e. when the effective rheology (3.12) is monotonic, the kinematic branch is unstable for large Reynolds numbers

$$Re > Re_{Kap} = \frac{3}{\left[(2+A)(2+A-2\alpha)+\alpha\right]\tan\theta}, \tag{3.26}$$

which extends the classical inertial Kapitza instability criteria to the shear-thickening rheology. In the Kapitza regime ($A > 0$), inertia introduces a lag, which tends to amplify kinematic waves, while gravity tends to spread and stabilize them. The instability arises when the speed of kinematic waves is larger than the speed of gravity waves (Whitham 2011). For a Newtonian fluid ($A = 1$ and $\alpha = 6/5$), the threshold of the Kapitza instability predicted by (3.26) is $1/\tan\theta$, which slightly overestimates the exact prediction $Re_{Kap,Newt} = (5/6)\tan\theta$ obtained from a rigorous long wave expansion of the Navier–Stokes equations (Benjamin 1957; Yih 1963). This well-documented discrepancy stems from assuming a fixed shape of the velocity profile. For a CST suspension ($0 < A < 1$), (3.26) predicts an increase in the critical Reynolds number relative to the Newtonian case. This is consistent with previous studies on power-law rheology fluids, which have shown that shear-thickening has a stabilizing effect on the flow (Hwang *et al.* 1994; Ng & Mei 1994).

For $A < 0$, i.e. when the effective flow rule (3.12) becomes negatively sloped, the stability condition is reversed. The kinematic branch is unstable for

$$Re < Re_{Kap} = \frac{3}{\left[(2+A)(2+A-2\alpha)+\alpha\right]\tan\theta}, \tag{3.27}$$

which means, surprisingly, that the kinematic branch is unstable at low Reynolds number, while inertia now has a stabilizing effect. This low Reynolds number instability, appearing

for a negatively sloped flow rule ($A < 0$), corresponds to the mechanism of formation of the Oobleck waves proposed by Darbois Texier *et al.* (2020). Indeed, in the limit of vanishing inertia ($Re = 0$), the dispersion relation (3.23) reduces to

$$\tilde{\omega} = (2 + A)\tilde{k} - \frac{A}{\tan\theta}\,\mathrm{i}\tilde{k}^2, \tag{3.28}$$

or equivalently, in the spatio-temporal domain,

$$\frac{\partial h_1}{\partial t} + (2 + A)\,\frac{\partial h_1}{\partial x} = \frac{A}{\tan\theta}\,\frac{\partial^2 h_1}{\partial x^2}. \tag{3.29}$$

One recognizes an advection–diffusion equation for the perturbative wave h_1, which predicts that waves propagate at the speed of kinematic waves $\tilde{c}_{kin} = 2 + A$, while diffusing with an effective diffusion coefficient $A/\tan\theta$. For $A < 0$, waves anti-diffuse, i.e. grow during propagation. As discussed in Darbois Texier *et al.* (2020), this instability can be understood, physically, as follows. In the absence of inertia, the balance of forces (3.11) between the gravity term, the basal stress and the pressure term implies that a locally positive (resp. negative) slope of the free surface causes a decrease (resp. increase) in the basal stress. Because of the negative slope of the flow rule ($A < 0$), the basal stress variation induces anti-correlated velocity variations (positive upstream of a bump, and negative downstream), which amplify the initial perturbation.

The analysis above confirms that although they are both kinematic modes, the extended Kapitza instability ($A > 0$) and Oobleck waves ($A < 0$) are fundamentally different. For the latter, the destabilizing mechanism is non-inertial and inertia has only a stabilizing effect, which stabilizes high Reynolds number flow.

The second branch, $\tilde{\omega}_2(\tilde{k})$, with growth rate $\tilde{\sigma}_2 = \mathrm{Im}(\tilde{\omega}_2) = -3\mathrm{i}/(A\,Re)$, is unstable only if $A < 0$, regardless of Reynolds number. The condition on A is the same as for Oobleck waves. However, the instability mechanism is, once again, fundamentally different. For the second branch, any perturbation is amplified when $A < 0$, independently of whether or not a free surface is present, because inertia introduces a mismatch between the basal stress and the driving gravity force. The branch is not specific to free-surface flows and disappears in the strict absence of inertia ($Re = 0$). For this reason, we call it the 'inertial branch'.

The two critical curves, $A = 0$ and $Re = Re_{Kap}$, lead to the stability diagram shown in figure 4, for an arbitrary plane inclination $\theta = 10^\circ$. For the sake of simplicity, the predictions are plotted for a fixed value of α (= 1, corresponding to a plug velocity profile). This simplification permits a two-dimensional representation, without altering the stability diagram, qualitatively. Note that the assumption $\alpha = 1$ is made only in figure 4, while the rest of the analysis considers the exact value of α obtained from (3.13). In this case, the critical Reynolds number of the kinematic branch reduces to $Re_{Kap} = 3/[(1 + A)^2 \tan\theta]$ (black solid line in figure 4*a*). As discussed above, the extended Kapitza instability develops for $A > 0$ and $Re > Re_{Kap}$, and Oobleck waves for $A < 0$ and $Re < Re_{Kap}$, whereas the inertial branch, shown in figure 4(*b*), is unstable for $A < 0$ and $Re > 0$.

To determine which criterion is reached first, and what instability is expected to be observed in practice, it is crucial to understand how Re and A vary in experiments given their coupled dependence on $\tau_{b,0}/\tau^*$, θ and ϕ. To this end, we display in figure 4 the trajectories followed by A and Re for an increasing flow rate (i.e. increasing $\tau_{b,0}/\tau^*$ or flow thickness) and a fixed angle ($\theta = 10^\circ$), which mimics the experimental protocol. The different trajectories correspond to different volume fractions, and the rheological parameters are those measured for the cornstarch suspensions (see § 2.1). Below ϕ_{DST}, the

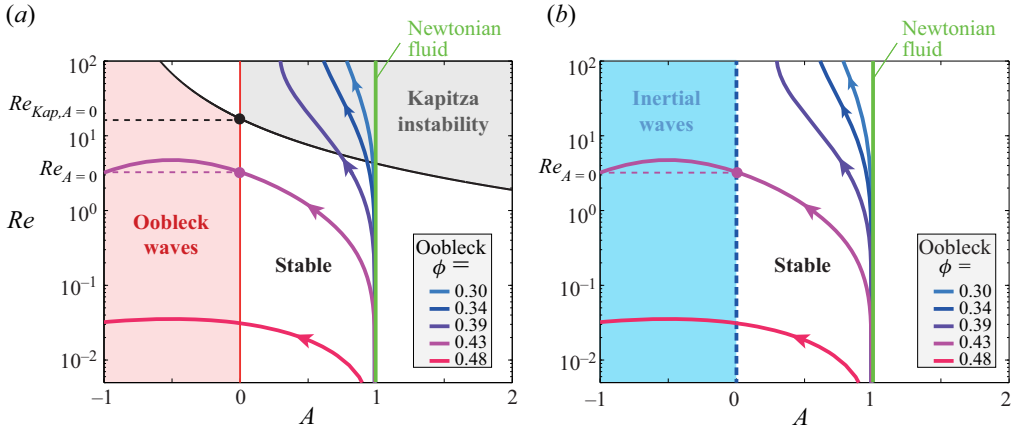

Figure 4. Stability diagram (Re, A) for (a) the kinematic branch, and (b) the inertial branch ($\theta = 10°$ and a plug flow profile, $\alpha = 1$, is assumed for simplicity; see text). (a) Black line: Kapitza instability threshold ($Re = Re_{Kap}$). Red line: Oobleck waves instability threshold ($A = 0$). (b) Dashed blue line: inertial branch instability threshold ($A = 0$). (a,b) The green line indicates the Newtonian case ($A = 1$). The coloured trajectories indicate the evolution of Re and A for various volume fractions and increasing flow rates (or basal stress $\tau_{b,0}$) ($\theta = 10°$, and the rheological parameters are those obtained from figure 1b). For most volume fractions above ϕ_{DST}, the DST condition $Re = Re_{A=0}$ (i.e. $A = 0$) is expected to be reached before (lower flow rate) the Kapitza instability onset ($Re = Re_{Kap}$).

trajectories only cross the $Re = Re_{Kap}$ critical line, since A remains strictly positive for all flow rates. This means that the Kapitza instability is expected, provided that the flow rate is increased sufficiently. By contrast, above ϕ_{DST}, one can, *a priori*, expect either the Kapitza instability or one of the two other instabilities (Oobleck wave and inertial branch), depending on which criterion ($A = 0$ or $Re = Re_{Kap}$) is reached first when the flow rate is increased. This condition is given by the respective value of the two Reynolds numbers defined by

$$Re_{A=0} \equiv \frac{3}{4}\frac{\tau_{b,A=0}^3}{\rho[g\,\eta(\phi,\,\tau_{b,A=0})\sin\theta]^2}, \quad \text{with } \mathcal{G}(\phi,\,\tau_{b,A=0}) = \frac{3}{2}, \tag{3.30}$$

corresponding to the intersection of the iso-ϕ trajectory with the vertical axis $A = 0$ (purple circle in figure 4), and

$$Re_{Kap,A=0} \equiv 3/[(4 - 3\alpha)\tan\theta], \tag{3.31}$$

corresponding to the intersection between the Kapitza threshold and the vertical axis $A = 0$ (black circle in figure 4). If $Re_{A=0} < Re_{Kap,A=0}$, as in figure 4, then the trajectory intersects the $A = 0$ criterion first, meaning that Oobleck waves and inertial branches are expected to be observed first, for an increasing flow rate. In the opposite case ($Re_{A=0} > Re_{Kap,A=0}$), the trajectory first encounters the Kapitza threshold (with A still positive), and the Kapitza instability is expected to develop first. The above condition between $Re_{A=0}$ and $Re_{Kap,A=0}$ involves ϕ non-trivially, the rheological parameters and the inclination angle θ. However, as figure 4 shows, for cornstarch and provided that the plane remains far from the vertical ($\theta \ll 90°$), the onset of DST ($A = 0$) is reached before the Kapitza threshold (Re_{Kap}) for almost all volume fractions above ϕ_{DST}.

In the following, the value of the Reynolds number when the first instability criterion is met for increasing flow rate and a fixed angle (i.e. following the iso-ϕ trajectories in

figure 4) will be denoted by Re_c, in order to match the experimental definition. In practice, for our range of parameters (cornstarch rheology, plane far from vertical), $Re_c = Re_{Kap}$ for $\phi < \phi_{DST}$, and $Re_c = Re_{A=0}$ for $\phi > \phi_{DST}$.

3.5. *Dispersion relation*

The previous analysis has focused on the limit of vanishing k. We now solve the dispersion relation exactly for an arbitrary wavenumber. The two solutions of (3.23) are

$$\tilde{\omega}_{1,2} = \frac{\dfrac{2\,Re}{3}\,\alpha\tilde{k} \pm \left(\dfrac{D+\sqrt{D^2+C^2}}{2}\right)^{1/2}}{\dfrac{2\,Re}{3}} + \mathrm{i}\,\frac{-\dfrac{1}{A} \pm \dfrac{C}{2}\left(\dfrac{2}{D+\sqrt{D^2+C^2}}\right)^{1/2}}{\dfrac{2\,Re}{3}}, \quad (3.32)$$

where $\pm$ stands for $+$ for the kinematic branch $\tilde{\omega}_1$, and $-$ for the inertial branch $\tilde{\omega}_2$, with

$$C = \frac{4\,Re}{3}\left(1 + \frac{2-\alpha}{A}\right)\tilde{k} \quad \text{and} \quad D = -\frac{1}{A^2} + \frac{4\,Re}{3}\left(\frac{Re}{3}\,\alpha(\alpha-1) + \frac{1}{\tan\theta}\right)\tilde{k}^2. \quad (3.33a,b)$$

Figures 5(*a*,*b*) present the growth rates for the two instabilities of the kinematic branch, namely, the Kapitza instability ($\phi = 0.33 < \phi_{DST}$, figure 5*a*) and the Oobleck wave instability ($\phi = 0.45 > \phi_{DST}$, figure 5*b*). The different colours stand for increasing values of Re close to Re_c (i.e. either Re_{Kap} or $Re_{A=0}$). For both instabilities, the growth rate is null for $\tilde{k} = 0$ and increases monotonically up to a plateau value at large $\tilde{k}$, which is the signature of a zero wavenumber instability. Interestingly, for a given wavenumber and distance to the threshold, the growth rate is several orders of magnitude larger for Oobleck waves than for the Kapitza instability (the vertical scale between the two panels differs by a factor 10^3). Figures 5(*c*,*d*) present the wave speeds of the two instabilities for the same parameters. Close to the instability threshold, the wave speed depends only weakly on $\tilde{k}$. It drops from approximately 3 for the Kapitza instability, to 2 for Oobleck waves, in agreement with the long wave limit $2 + A$, since $A \simeq 1$ at the Kapitza threshold and $A = 0$ at the Oobleck waves threshold.

The growth rate of the inertial branch is shown in figures 6(*a*,*b*) for the same set of ϕ and Re/Re_c as previously. We recover that the branch is unconditionally stable below ϕ_{DST}, and unstable above ϕ_{DST} for Reynolds numbers larger than $Re_{A=0}$. By contrast with the kinematic branch, the growth rate is non-null at $\tilde{k} = 0$ and actually diverges at the instability threshold ($A = 0$), where it changes sign, before decreasing with increasing Re above the threshold. The corresponding wave speeds are presented in figures 6(*c*,*d*). For $\phi > \phi_{DST}$, the wave speed at threshold is lower than for the kinematic branch. Although the kinematic and inertial branches share the same criterion of stability for concentrated suspensions ($A = 0$), the comparison between figures 5 and 6 suggests that they differ strongly in terms of growth and propagation speed. We address this point in the next section, where we compare predictions with experiments.

4. Comparison with experiments

4.1. *Stability threshold*

We compare, first, the stability criteria derived above with the wave onset conditions observed in experiments and detailled in Appendix A. Figure 7(*a*) presents $Re_c/Re_{Kap,Newt}$,

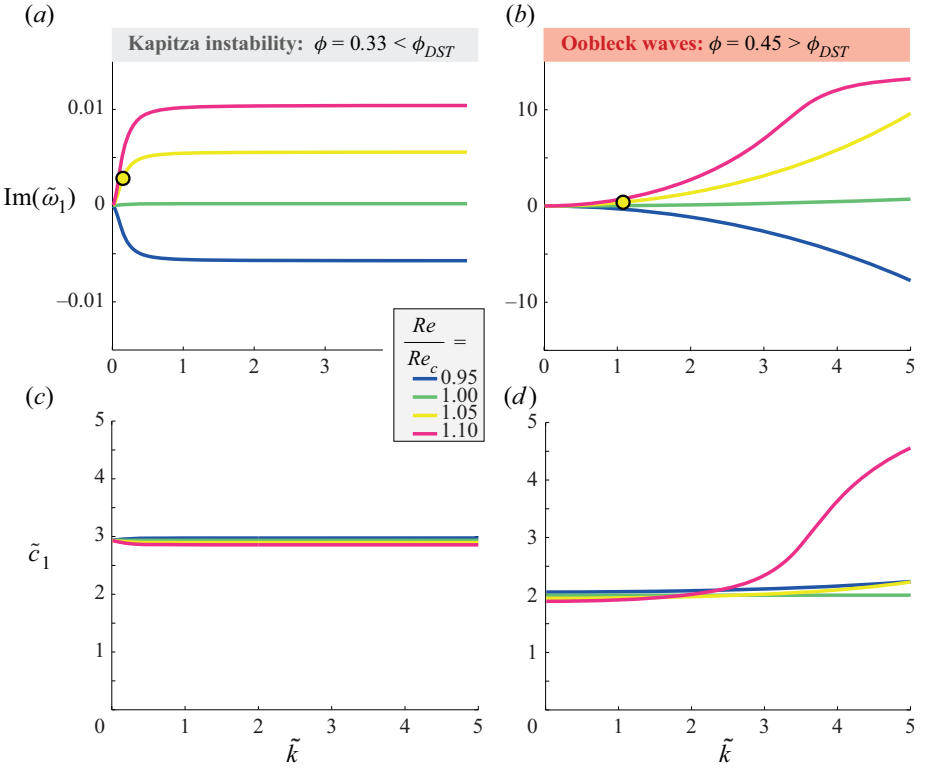

Figure 5. Dispersion relations of the two instabilities of the kinematic branch ($\theta = 10°$). (*a*,*c*) Kapitza instability ($\phi = 0.33$). (*b*,*d*) Oobleck waves instability ($\phi = 0.45$). (*a*,*b*) Temporal growth rate $\mathrm{Im}(\tilde{\omega}_1)$. Note the highly different scales of the *y*-axis. (*c*,*d*) Wave speed $\tilde{c}_1$. (*a–d*) The yellow circles indicate the theoretical growth rates, for $Re = 1.05\,Re_c$ and at the wavelength observed experimentally, which are compared with measurements in figure 8(*b*).

i.e. the critical Reynolds number normalized by that for a Newtonian liquid ($Re_{Kap,Newt} = (5/6)/\tan\theta$; see § 3.4), as a function of ϕ, whereas figure 7(*b*) reports the critical basal shear stress τ_c, also versus ϕ. The symbols represent the experimental measurements for various volume fractions. Each one is obtained by varying the flow rate at a fixed inclination of the plane (encoded by the shape of the symbol), as detailed in § 2. The solid lines represent the theoretical predictions for the same protocol, i.e. the critical Reynolds number Re_c at which each iso-ϕ trajectory (see figure 4) reaches the $Re = Re_{Kap}$ or $Re = Re_{A=0}$ condition. The relative threshold $Re_c/Re_{Kap,Newt}$ is close to 1 at low volume fraction, where shear-thickening is mild, and increases with increasing ϕ to reach $\simeq 6$ at $\phi = 0.41 \simeq \phi_{DST}$. This illustrates the significant stabilization effect of CST in the Kapitza regime, in fair agreement with the evolution of Re_{Kap} predicted by (3.26) (solid black line in figure 7*a*). Similarly, the steep increase in the critical stress τ_c, which is observed experimentally close to $\phi = 0.41$ (figure 7*b*), agrees with the expected divergence of the effective viscosity coefficient of the flow, $\mathrm{d}\tau_{b,0}/\mathrm{d}\dot{\gamma} \propto A^{-1}$, in $\phi_{DST} \simeq 0.41$. This confirms the Kapitza-like nature of the instability (destabilizing inertia versus stabilizing gravity) below ϕ_{DST}.

Above ϕ_{DST}, both the critical Reynolds number and the critical shear stress observed experimentally drop drastically, by up to two orders of magnitude, for Re_c, at $\phi = 0.47$

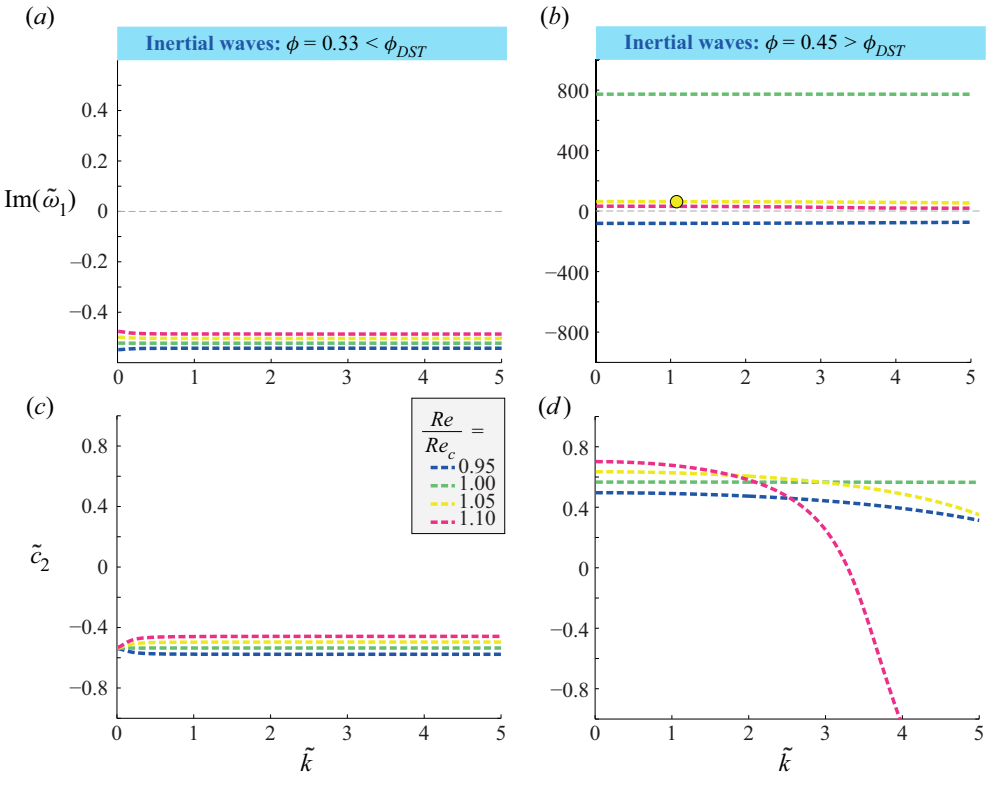

Figure 6. Dispersion relation of the inertial branch ($\theta = 10^\circ$): (a,c) $\phi = 0.33$, (b,d) $\phi = 0.45$. (a,b) Temporal growth rate $\mathrm{Im}(\tilde{\omega}_2)$. ($c$,$d$) Wave speed $\tilde{c}_2$. The yellow circle indicates the theoretical growth rates, for $Re = 1.05\,Re_c$ and at the wavelength observed experimentally, which are compared with measurements in figure 8(b).

(figure 7a). The drop in Re_c is captured correctly by the theoretical prediction $Re_c = Re_{A=0}$ of (3.30), which, once again, applies to both Oobleck waves and the inertial waves instability, and does not permit us to distinguish between them. The agreement is also reasonable when the instability threshold is expressed in terms of τ_c, although the prediction underestimates the measured value by approximately a factor 2 (figure 7b). To clarify this discrepancy, we note that the theoretical prediction relies on the value of the rheological parameters (η_s, ϕ_0, ϕ_1 and τ^*) as obtained from the cylindrical Couette rheometry (see § 2.1). In the inset of figure 7(b), we test these parameters more directly versus the inclined flow configuration by comparing the depth-averaged flow rule, $\tau_{b,0}$ versus u_0/h_0, that they predict, (3.7), with the one measured directly in the experiments on the incline. A significant difference is observed between the two flow rules, showing that the steady uniform flow down the incline is not well predicted from the rheological parameters obtained with the Couette rheometer. Such a difference has been reported previously in the case of non-shear-thickening suspensions (Bonnoit *et al.* 2010) and could arise from the modification of the velocity profile due to particle migration effects, which are not considered here (see § 3.1). Remarkably, however, when the expression for the critical shear stress τ_c is computed from the flow rule measured with the inclined plane (i.e. from the points $\mathrm{d}\dot{\gamma}/\mathrm{d}\tau_{b,0} = 0$ highlighted by the black crosses in the inset of figure 7b), the agreement between the theoretical predictions and measurements becomes quantitative

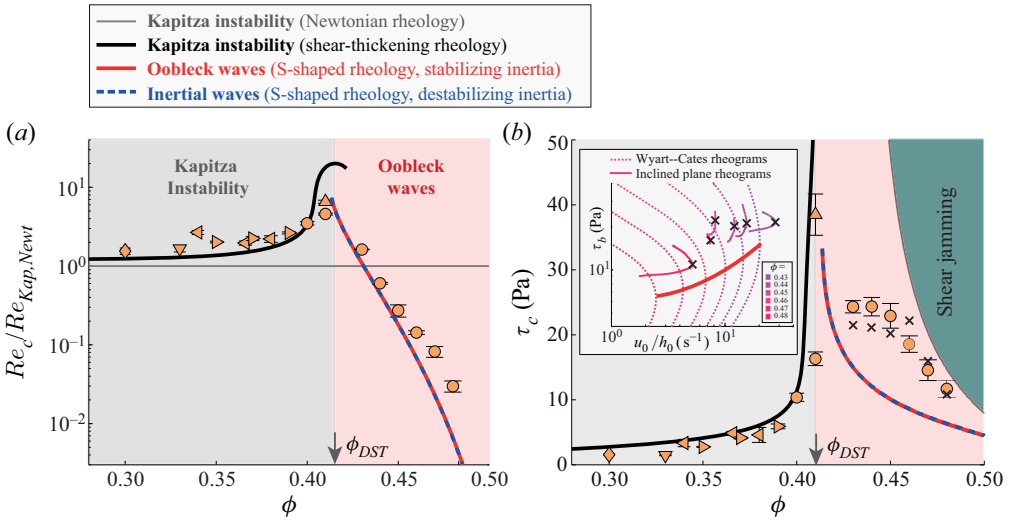

Figure 7. Destabilization threshold: comparison with experiments. (*a*) Critical Reynolds number Re_c normalized by the Newtonian Kapitza threshold $Re_{Kap,Newt} = (5/6)/\tan\theta$ versus volume fraction ϕ. (*b*) Critical basal shear stress τ_c versus ϕ. The symbols indicate measurements. Their shapes encode the inclination θ: $\diamond$ 2°, $\triangledown$ 3°, $\triangleright$ 6°, $\triangleleft$ 9°, $\circ$ 10°, $\triangle$ 22°. The error bars indicate the standard deviation of the measurements at a given ϕ. The lines represent the predictions for the different modes (as labelled above the graph), i.e. the critical Reynolds number at which each iso-ϕ trajectory (see figure 4) reaches the $Re = Re_{Kap}$ or $Re = Re_{A=0}$ condition. (The black line is interrupted above $\phi \simeq 0.42$ since no steady flow verifies $Re = Re_{Kap}$.) The shear-jamming limit corresponds to the value of the basal shear stress when the flow first jams at $z = 0$ (see (3.5)). Inset: basal shear stress $\tau_{b,0} = \rho g h_0 \sin\theta$ versus mean shear rate u_0/h_0 for different volume fractions obtained from Wyart–Cates rheological laws (dashed lines) and from direct measurements on the inclined plane (solid lines). The red line and black crosses highlight the condition $\mathrm{d}\tau_b/\mathrm{d}\dot{\gamma} = 0$ for both sets of curves.

(crosses versus orange symbols in figure 7*b*). This suggests that the mild quantitative discrepancy between theory and experiments for τ_c stems not from a limitation of the linear stability analysis but rather from the calibration of the base flow itself.

The comparison above confirms that the onset of a negatively sloped flow rule ($A = 0$) is, experimentally, the condition for flow stability above ϕ_{DST}. However, it does not allow us to determine which of the kinematic branch or inertial branch is observed. To do so, the predictions for the growth rate and celerity of the waves, which differ between the two instability mechanisms, have to be compared with experiments.

4.2. *Wave speed and growth rate*

Figure 8(*a*) reports the wave speed, at the instability threshold, measured for various volume fractions. The ratio c_c/u_c is almost constant around 3 at low volume fractions, decreases to approximately 2 between $\phi \simeq 0.37$ and $\phi = 0.41 \simeq \phi_{DST}$, and decreases further, a little below 2, for higher ϕ. This behaviour agrees well with the prediction of the shear-thickening Kapitza regime expected below ϕ_{DST} (black solid line). Above ϕ_{DST}, the measurements are found to match the prediction $\tilde{c}_c = 2$ for the kinematic branch better than the prediction $\tilde{c}_c = 2(\alpha - 1) \simeq 0.6$ for the inertial branch, which suggests that the mechanism of the instability observed in experiments is that of Oobleck waves, rather than that of the inertial branch instability. This result is confirmed by a direct comparison between the measured wave speed and the speed of the kinematic waves $c_{kin} \equiv \mathrm{d}q/\mathrm{d}h_0$,

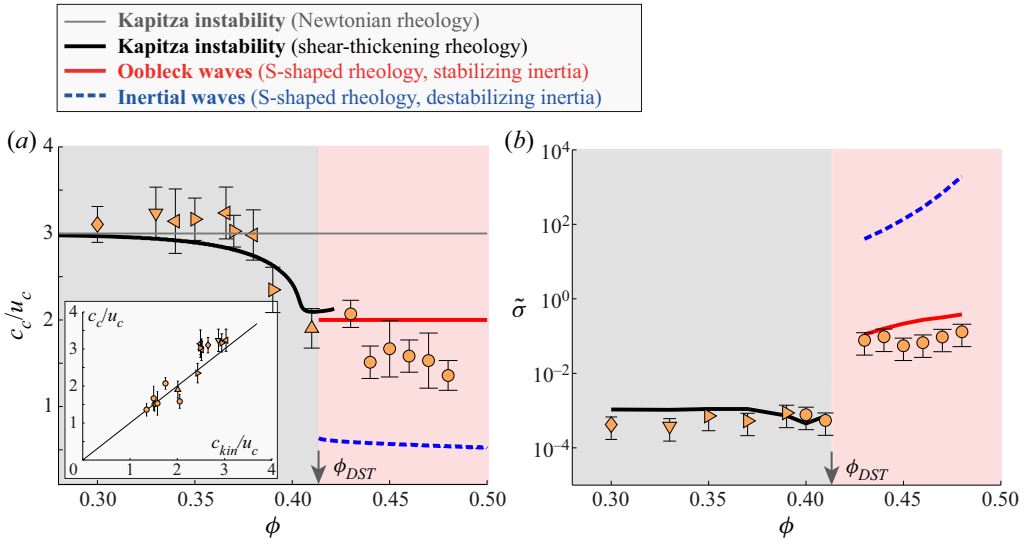

Figure 8. Wave speed and growth rate: comparison with experiments. (*a*) Wave speed c_c normalized by the mean fluid velocity u_c at the instability onset versus ϕ. Inset: normalized wave velocity c_c/u_c versus normalized speed of kinematic waves c_{kin}/u_c at the onset. (*b*) Normalized spatial growth rate $\tilde{\sigma}$ versus ϕ for $Re/Re_c = 1.05$.

as deduced from the experimental base flow measurements. As shown in the inset of figure 8(*a*), c_c is fairly close to c_{kin} over the whole range of volume fraction studied.

The growth rates of the instability are compared in figure 8(*b*). The measurements are performed when the Reynolds number of the flow is 5 % above the observed critical value ($Re/Re_c = 1.05$). The theory is computed for the wavelength observed experimentally at each ϕ (see figures 5 and 6). Here again, below ϕ_{DST}, the growth rate is predicted correctly by the Kapitza instability accounting for continuous thickening (black solid line). Above ϕ_{DST}, the prediction for the kinematic branch (red solid line) matches the measurements fairly well, whereas that for the inertial branch (blue dashed line) overestimates the observed growth rate by approximately two orders of magnitude.

The previous results indicate that including inertia in the depth-averaged analysis provides a fair description for both the shear-thickening Kapitza regime observed below ϕ_{DST} and the low Reynolds number Oobleck wave regime observed above ϕ_{DST}. Nonetheless, one important question remains. Above ϕ_{DST}, the inertial branch has the same instability condition as Oobleck waves, but since the former is expected to amplify two orders of magnitude faster (see figure 8*b*), why do we not observe, experimentally, the inertial mode rather than Oobleck waves?

5. Role of a delay in the rheology

To explain the apparent paradox of the sub-dominance of the inertial branch above ϕ_{DST}, it is important to realize that the inertial mode in the previous analysis has a singular behaviour. It disappears in the strict absence of inertia, but its growth rate diverges as the Reynolds number tends to zero (see (3.25)). This singularity at $Re = 0$ results from the assumption of a steady flow rule, which implies that viscosity adapts to change in stress, instantaneously. In reality, when a shear-thickening suspension flow is perturbed, a finite strain γ_0 is required to relax the fraction of frictional contacts f (hence the viscosity) to the new steady-state value (Mari *et al.* 2015*b*; Chacko *et al.* 2018; Han *et al.* 2018; Richards

et al. 2019). As shown in previous studies, this delay in the rheology may strongly modify the stability of the flow in the negatively sloped region (Nakanishi & Mitarai 2011; Chacko *et al.* 2018; Richards *et al.* 2019). For instance, in the case of a simple shear flow driven by a heavy rheometric tool, the addition of a delay stabilizes the flow, by shifting the instability condition on $\mathrm{d}\dot{\gamma}/\mathrm{d}\tau$ towards negative values (Richards *et al.* 2019).

To study the influence of a strain delay on our predictions, we extend the linear stability analysis of § 3 by adding an evolution equation for the fraction f of frictional contacts. Following Mari *et al.* (2015*b*), Han *et al.* (2018), Chacko *et al.* (2018) and Richards *et al.* (2019), we assume

$$\frac{\mathrm{d}f}{\mathrm{d}t} = -\frac{\dot{\gamma}}{\gamma_0}\,(f - f_{eq}), \tag{5.1}$$

where $f_{eq} = \mathrm{e}^{-\tau^*/\tau}$ is the equilibrium value of f, obtained for a steady flow, and γ_0 is a relaxation strain, whose typical value for frictional spheres is $\sim 10^{-2}$–10^{-1} (Mari *et al.* 2015*b*; Chacko *et al.* 2018; Richards *et al.* 2019). The details of the stability analysis are given in Appendix B. We discuss here only the main predictions. The first consequence of the introduction of a delay is to lead to three modes instead of two. One of them is a modified kinematic mode, and the other two are derived from the former inertial branch.

The stability diagram of the modified kinematic mode is shown in figure 9(*a*). In the long-wavelength limit ($\tilde{k} \to 0$) and for a small delay ($\gamma_0 \tan\theta \ll 1$), the instability thresholds are set by the following Reynolds number and critical value of A:

$$Re_{Kap}^{\gamma_0} \simeq \left(1 + \frac{\gamma_0 \tan\theta}{2A}\,(2 - A - A^2)\right) Re_{Kap} \quad \text{and} \quad A_- \simeq -\gamma_0 \tan\theta. \tag{5.2a,b}$$

For $A > 0$, we recover a Kapitza regime above the modified critical Reynolds number $Re_{Kap}^{\gamma_0}$, which is shifted relative to the zero-delay threshold Re_{Kap}. The delay also shifts slightly the criterion for Oobleck waves, which is now given by $Re < Re_{Kap}^{\gamma_0}$ and $A < A_-$ (instead of $A < 0$ without delay). As a result, there exists a narrow range of negative value of A ($A_- < A < 0$), between the Kapitza and the Oobleck waves instabilities, where the flow is always stable. Therefore, the addition of a small strain delay in the rheology slightly stabilizes Oobleck waves but it does not change the properties of the kinematic mode relative to the case without delay, significantly. This is confirmed by verifying that the wave speed in the long wave limit still has the expression for kinematic waves, $\tilde{c}_{kin} = 2 + A$ (see Appendix B), as was the case without delay.

The conclusion is different for the inertial mode, which is now twofold in the presence of a delay. In the long wave ($\tilde{k} \to 0$) and small delay ($\gamma_0 \tan\theta \ll 1$) limit, these two modes are unstable for

$$A < A_c = -\frac{3\gamma_0}{2\,Re}. \tag{5.3}$$

This instability threshold is similar to that obtained by Mari *et al.* (2015*b*) and Richards *et al.* (2019) (and previously by Nakanishi & Mitarai (2011) using a different S-shape rheology) when considering the influence of a delay on the stability of a simple shear flow in the DST regime. However, it differs strongly from the simple $A < 0$ condition without delay, as illustrated in the stability diagram of the inertial mode presented in figure 9(*b*). In the negatively sloped region ($A < 0$), there is now a large domain of stability, which is all the more extended for a low inertia and long delay. Importantly, the addition of a delay also removes the singularity of the inertial mode at $Re = 0$ discussed above. The growth rate now vanishes at the stability threshold instead of diverging (see (B 18) in Appendix B).

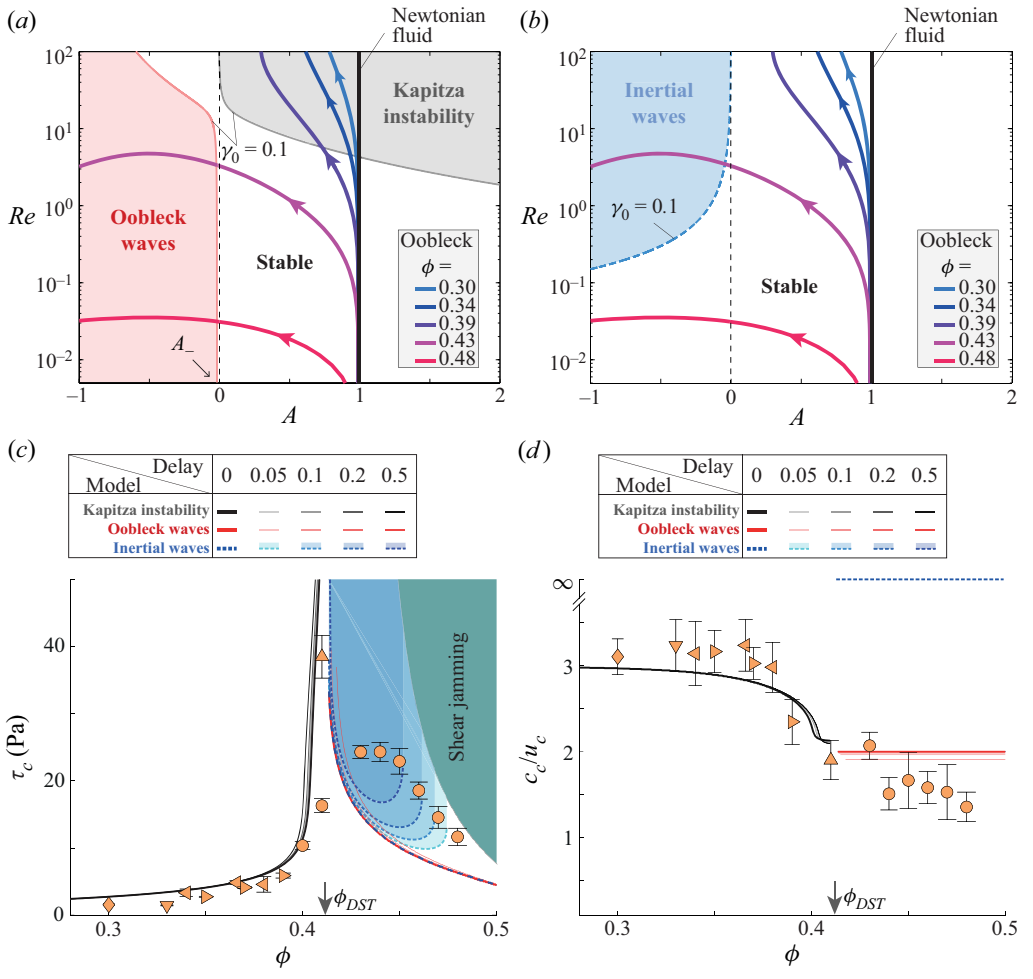

Figure 9. Role of a strain delay on stability. Stability diagrams (Re, A) for (a) the kinematic branch and (b) the inertial branch ($\theta = 10°$, $\alpha = 1$). (a) The grey and red domains indicate the unstable regions for $\gamma_0 = 0.1$. (b) The blue dashed line is the instability threshold (5.3) for $\gamma_0 = 0.1$. The coloured lines indicate the system trajectories for increasing flow rate at fixed angle (as in figure 4). The vertical dark lines indicates the Newtonian case ($A = 1$). (c) Critical shear stress τ_c, and (d) normalized wave velocity c_c/u_c at the threshold, versus ϕ. The symbols report the measurements presented in figures 7(b) and 8(c). The black and red lines indicate the predictions for the kinematic branch below and above ϕ_{DST}, respectively. The blue lines show the predictions for the inertial branch. The colour intensities of the lines correspond to delay strains of $\gamma_0 = 0.05, 0.1, 0.2$ and 0.5.

This means that slightly above the threshold, the inertial mode grows slowly and not several orders of magnitude faster than the kinematic mode, as predicted in the case without delay. Finally, the addition of a delay also changes qualitatively the frequency of the inertial mode in the long wave limit. Instead of vanishing as $\mathrm{Re}(\tilde{\omega}) \propto \tilde{k}$, the frequency at threshold with delay remains finite at $\tilde{k} = 0$ and is given by $\mathrm{Re}(\tilde{\omega}) \simeq \sqrt{6/(\gamma_0 Re)} \simeq (2/\gamma_0)\sqrt{-A_c}$. Thus the long wave limit of the inertial modes with delay is an oscillatory instability, with a wave speed diverging in $\tilde{k} \to 0$. Overall, these results for the inertial modes at $\tilde{k} \to 0$ recover the purely temporal analysis performed by Richards *et al.* (2019) in the case of a confined Couette flow.

As previously, the onset of instability in the experiments (where the flow rate, hence τ_b, is slowly varied) is expected at the intersection between the critical stability curves and the system trajectories in the A–Re plane for fixed ϕ and θ. For $\phi < \phi_{DST}$, the Kapitza regime is expected, with an onset at $Re = Re^{\gamma_0}_{Kap}(A)$ (see (5.2*a*,*b*)). For $\phi > \phi_{DST}$, the onset of instability is expected at $A = A_-(Re)$ for the kinematic branch, and $A = -3\gamma_0/(2\,Re)$ for the inertial branches. These predictions are plotted in terms of the critical shear stress in figure 9(*c*) for four values of the strain delay $\gamma_0 = 0.05, 0.1, 0.2$ and 0.5, that bound the experimental value determined by Richards *et al.* (2019). The colour intensity of the lines corresponds to increasing values of the delay, and the darkest colour recalls the stability threshold without delay ($\gamma_0 = 0$). We recover the weak influence of the delay on the onset of the kinematic branch mentioned in the previous discussion, as well as the strong shift in the predicted critical shear stress τ_c for the inertial branches, which is observed to increase with γ_0.

Remarkably, for volume fractions sufficiently above ϕ_{DST}, the inertial mode is stable whatever the basal stress (see the shift of the right-hand boundary of the blue domains in figure 9*c*), although the slope of the flow rule reaches strongly negative values. This is because the Reynolds number decreases at large basal stress for these high values of ϕ, such that the trajectory never reaches the stability threshold $A_c = -3\gamma_0/(2\,Re)$ (for the inclination $\theta = 10^\circ$ considered, which is representative of the experimental range 2°–22°). Clearly, this predicted stabilization of the inertial mode at high volume fraction does not match experiments, where waves are all the more unstable as the volume fraction is high. By contrast, no band of unconditionally stable volume fractions is expected for Oobleck waves (see the red curves in figure 9*c*), which match the observations. Another important difference concerns the wave velocity (figure 9*d*), which is predicted to diverge for the inertial branches with delay (blue dashed line), in stark contrast with the prediction for the kinematic mode, which is not far from experimental observation.

These considerations shed some light on the paradox of the sub-dominance of the inertial modes above ϕ_{DST}. While a strain delay γ_0 in the rheology modifies the kinematic mode only marginally, it may turn the inertial modes stable even for largely negatively sloped flow rules, provided that the Reynolds number is low enough (which is all the more true as ϕ exceeds ϕ_{DST} largely). More precisely, comparing (5.2*a*,*b*) with (5.3) indicates that inertial waves are expected before Oobleck waves ($3\gamma_0/(2\,Re) < \gamma_0 \tan\theta$) only for $Re/Re_{Kap,Newt}$ above $9/5$, and regardless of the value assumed for γ_0. Given the smallness of the critical Reynolds numbers actually observed (see figure 7), this suggests that Oobleck waves dominate the inertial modes for most of the volume fractions above ϕ_{DST}, which would explain the experimental observations. Another possibility is that the two modes actually coexist but the inertial modes are not detected in our measurements. Indeed, since Oobleck waves are a zero wavenumber instability with finite wave velocity, while the inertial modes are an oscillatory instability, the two instabilities are presumably decoupled both spatially and temporally. Therefore, it is possible that the inertial mode is related to the high-frequency 'jittering' reported by Balmforth *et al.* (2005), which is not characterized in our experiments. However, such a statement would require more investigations that could be the topic of future studies.

6. Conclusion

This study has addressed the stability of a free-surface layer flow of a shear-thickening suspension down an incline. It has shown that the onset of instability and the main characteristics of the waves observed experimentally close to the onset can be rationalized,

on the basis of a depth-averaged analysis considering Wyart–Cates effective rheology and inertia, in the different regimes where the flow is continuously shear-thickening, discontinuously shear thickening, or shear jamming.

Below the onset particle volume fraction for DST, ϕ_{DST}, the analysis predicts a modified Kapitza (roll-wave) instability of inertial origin, which develops above a critical Reynolds number Re_{Kap}, increasing with increasing ϕ, as a result of the CST of the suspension, and which propagates at the velocity of kinematic waves, in good agreement with experimental observations.

Above ϕ_{DST}, two other unstable branches are identified, which both stem from the negative slope of the suspension flow rule ($A \equiv \mathrm{d}\dot{\gamma}/\mathrm{d}\tau < 0$) when the bottom of the flow shear-thickens discontinuously. They have, consequently, the same critical Reynolds number $Re_{A=0}$, or critical shear-stress $\tau_{b,A=0}$, set by $A = 0$ (which are lower than the Kapitza threshold values for most of the volume fractions above ϕ_{DST} for cornstarch and provided that the plane is far from vertical, $\theta \ll 90°$). Nonetheless, the mechanisms behind these two branches are fundamentally different. The 'kinematic branch' is an amplification of kinematic surface waves due to a mismatch between the free-surface deformation and the basal stress rheology. For a negatively sloped rheology, this branch is unstable when $Re < Re_{Kap}$, does not require inertia, and corresponds to the Oobleck waves instability identified in Darbois Texier *et al.* (2020) from the analysis conducted at $Re = 0$. By contrast, the 'inertial branch' results from the acceleration of the flowing layer when the basal stress is velocity-weakening. It requires a negatively sloped rheology and inertia, but no coupling with the free-surface deformation. These different instability mechanisms yield very different predictions for the growth and propagation of the waves. Those for the Oobleck wave mechanism match the measured wave speed and growth rate much better than those for the inertial branch instability, which supports the mechanism of Oobleck wave formation proposed in Darbois Texier *et al.* (2020). This conclusion is confirmed by extending the stability analysis to a modified shear-thickening law including a strain delay, which has been shown to have important consequences for the stability of other shear-thickening flows (Nakanishi & Mitarai 2011; Mari *et al.* 2015*b*; Chacko *et al.* 2018; Han *et al.* 2018; Richards *et al.* 2019). The addition of a delay is found to modify only slightly the predictions for Oobleck waves, which still agree with measurements, whereas it predicts a strong stabilization of the inertial branch at large volume fraction, where the instability is still observed experimentally.

Overall, this study confirms that the non-inertial Oobleck wave mechanism proposed in Darbois Texier *et al.* (2020) is at the origin of the wave formation above ϕ_{DST}, and not inertial modes studied in previous works (Mari *et al.* 2015*b*; Richards *et al.* 2019). To our knowledge, the only other inertialess mechanism reported so far in shear-thickening suspensions is a dynamic vorticity banding instability observed in overdamped discrete numerical simulations (Chacko *et al.* 2018). However, unlike the Oobleck wave mechanism, this instability (i) develops in the direction transverse to the flow, (ii) requires a velocity-driven configuration (as opposed to the stress-driven configuration of the inclined plane), and (iii) requires that an extra order parameter be added to the flow rule, such that $\dot{\gamma}$ and τ are not instantaneously related.

Developments remain needed to obtain a complete description of shear-thickening waves. Extending the (one-dimensional) depth-averaged linear analysis to two dimensions would be needed to capture the correct dissipation at short wavelength. A further extension would be to relax the assumption of a constant volume fraction and account for particle migration induced by the inhomogeneous stress profile in the stability analysis, in order to seek possible new stabilizing or destabilizing mechanisms (Carpen & Brady 2002; Chacko

et al. 2018; Dhas & Roy 2022). Also, waves quickly become highly nonlinear, especially in the DST regime (see figure 2*a*), and investigating experimentally and theoretically the properties of large amplitude waves, or solitons, would be relevant. The theoretical part of this extension would require considering the effect of higher-order terms in the wave dynamics equations. More generally, this study shows the relevance of S-shape constitutive rheological laws for predicting novel hydrodynamic instabilities in shear-thickening suspensions. It also emphasizes the variety of the instability mechanisms resulting from such a rheology, which could be increased by addressing the case of capillary flows, where subtle stabilizing effects can be expected. Finally, beyond shear-thickening suspensions, the theoretical framework adopted in this study could be applied to other complex fluids showing a non-monotonic effective flow curve down slopes, which may be found in geophysical and industrial contexts.

Funding. This work was supported by the European Research Council under the European Union Horizon 2020 Research and Innovation programme (ERC grant agreement no. 647384) and by ANR ScienceFriction (ANR-18-CE30-0024).

Declaration of interests. The authors report no conflict of interest.

Author ORCIDs.
Henri Lhuissier https://orcid.org/0000-0002-8586-8153;
Bloen Metzger https://orcid.org/0000-0003-3031-6543;
Yoël Forterre https://orcid.org/0000-0001-6052-7291.

Appendix A. Experimental data

This appendix compiles the experimental data obtained for the destabilization of the cornstarch suspension flow down the inclined plane. Table 1 lists, for each experiment, the following quantities: the suspension volume fraction ϕ, the slope angle θ, the Kapitza criterion Re_{Kap}, the critical flow thickness h_c, the critical mean flow velocity u_c, the critical Reynolds number Re_c, the ratio Re_c/Re_{Kap}, the critical basal shear stress τ_c, the critical wave speed c_c, the ratio c_c/u_c, the normalized critical kinematic speed c_{kin}/u_c, and the normalized growth rate $\tilde{\sigma}$ for $Re = 1.05\,Re_c$.

Appendix B. Linear stability analysis with a strain delay

This appendix details the linear stability analysis for the Wyart–Cates rheology with a strain delay γ_0.

First, the effective basal rheology (3.12) is written in terms of the fraction of frictional contact f_b at the wall ($z = 0$):

$$\frac{\bar{u}}{h} = \frac{\tau_b}{3\,\eta(f_b)}\,\mathcal{G}_2(f_b) \equiv \dot{\Gamma}(\tau_b, f_b), \tag{B1}$$

where $\eta(f_b) = \eta_s(\phi_J(f_b) - \phi)^{-2}$ is the viscosity, $\phi_J(f_b) = \phi_0(1 - f_b) + \phi_1 f_b$ is the critical volume fraction, and $\mathcal{G}_2(f_b)$ is a dimensionless corrective factor accounting for the shape of the velocity profile, such that for a steady flow, $f_b = f_{eq}(\tau_b) = \mathrm{e}^{-\tau^*/\tau_b}$ and $\mathcal{G}_2(f_b) = \mathcal{G}(\tau_b)$. Then we express the evolution equation (5.1) for the fraction of frictional

https://doi.org/10.1017/jfm.2023.162 Published online by Cambridge University Press

ϕ	θ (deg.)	Re_{Kap}	h_c (mm)	u_c (cm s^{-1})	Re_c	Re_c/Re_{Kap}	τ_c (Pa)	c_c (cm s^{-1})	c_c/u_c	c_{kin}/u_c	$\tilde{\sigma}$
0.30	2	23.9	3.91	12.9	37.0	1.55	1.56	39.9	3.10	2.65	4.2×10^{-4}
0.33	3	15.9	2.45	10.2	26.4	1.66	1.46	32.9	3.23	2.76	3.8×10^{-4}
0.34	9.3	5.1	1.78	11.5	13.6	2.67	3.35	36.1	3.14	2.49	—
0.35	6	7.9	2.26	11.1	16.0	2.02	2.76	35	3.16	2.94	7.2×10^{-4}
0.366	9.3	5.1	2.55	11.6	9.9	1.96	4.85	36.8	3.24	3.03	—
0.37	6	7.9	3.40	14.3	17.8	2.24	4.14	43.3	3.03	2.49	5.3×10^{-4}
0.38	9.3	5.1	2.40	11.2	11.2	2.21	4.60	33.3	2.98	2.51	—
0.39	6	7.9	4.75	18.4	20.9	2.63	5.91	43.0	2.35	3.10	8.7×10^{-4}
0.40	10	4.7	5.00	22.2	16.5	3.49	10.4	40.2	1.81	2.05	7.7×10^{-4}
0.41	10	4.7	7.82	30.7	21.6	4.57	16.3	—	—	—	5.4×10^{-4}
0.414	22	2.06	8.60	37.7	13.5	6.56	38.5	71.7	1.90	2.01	—
0.43	10	4.7	11.55	22.4	7.66	1.62	24.3	46.4	2.07	1.75	7.7×10^{-2}
0.44	10	4.7	11.51	13.6	2.84	0.60	24.3	20.6	1.51	1.52	9.6×10^{-2}
0.45	10	4.7	10.79	8.9	1.29	0.27	22.9	14.8	1.67	1.53	5.5×10^{-2}
0.46	10	4.7	8.70	5.7	0.66	0.14	18.6	9.0	1.58	2.05	6.7×10^{-2}
0.47	10	4.7	6.79	3.9	0.39	0.08	14.6	5.9	1.53	1.58	9.5×10^{-2}
0.48	10	4.7	5.42	2.1	0.13	0.03	11.7	2.8	1.37	1.35	1.3×10^{-1}

Table 1. Experimental data for surface destabilization of a flow of cornstarch suspension down an inclined plane.

contact at the bottom of the flowing layer as

$$\frac{\partial f_b}{\partial t} + u_b \frac{\partial f_b}{\partial x} = -\frac{\dot\gamma_b}{\gamma_0}\left[f_b - f_{eq}(\tau_b)\right], \tag{B2}$$

where $u_b = 0$ is the velocity at the wall (no-slip condition), and $\dot\gamma_b$ is the shear rate at the wall. Writing the flow rule at the bottom as $\tau_b = \eta(f_b)\,\dot\gamma_b$, and identifying with (B1), gives $\dot\gamma_b = (3/\mathcal{G}_2(f_b))\bar u/h$.

Normalizing and linearizing (B1) and (B2) together with the mass and momentum equations (3.10)–(3.12) around the base state, using $\tilde x = x/h_0$, $\tilde t = t\,\bar u_0/h_0$, $\tilde{\dot\Gamma} = \dot\Gamma h_0/\bar u_0$, $\tilde h = h/h_0 = 1 + h_1$, $\tilde u = \bar u/\bar u_0 = 1 + u_1$, $\tilde\tau_b = \tau_b/\tau_{b,0} = 1 + \tau_1$ and $f_b = f_{eq}(\tau_{b,0}) + f_1$, with $|h_1|, |u_1|, |\tau_1|, |f_1| \ll 1$, gives

$$\frac{\partial h_1}{\partial \tilde t} + \frac{\partial h_1}{\partial \tilde x} + \frac{\partial u_1}{\partial \tilde x} = 0, \tag{B3}$$

$$\frac{Re}{3}\left[\frac{\partial u_1}{\partial \tilde t} + (\alpha - 1)\frac{\partial h_1}{\partial \tilde x} + (2\alpha - 1)\frac{\partial u_1}{\partial \tilde x}\right] = h_1 - \tau_1 - \frac{1}{\tan\theta}\frac{\partial h_1}{\partial \tilde x}, \tag{B4}$$

$$u_1 - h_1 = \tau_1 + \left(\frac{\partial \tilde{\dot\Gamma}}{\partial f_b}\right)_0 f_1, \tag{B5}$$

$$\frac{\partial f_1}{\partial \tilde t} = -\frac{1}{\gamma_0^\star}\left[f_1 - \left(\frac{\mathrm{d}f_{eq}}{\mathrm{d}\tilde\tau_b}\right)_0 \tau_1\right], \tag{B6}$$

where $\gamma_0^\star = \gamma_0\,\mathcal{G}(\tau_{b,0})/3$. Making use of $\dot\Gamma = u/h$, the equations can be recast into the following linear system of h_1, $\dot\Gamma_1 = u_1 - h_1$ and f_1:

$$\frac{\partial h_1}{\partial t} + 2\frac{\partial h_1}{\partial x} + \frac{\partial \dot\Gamma_1}{\partial x} = 0, \tag{B7}$$

$$\frac{Re}{3}\left(\frac{\partial \dot\Gamma_1}{\partial \tilde t} + 2(\alpha - 1)\frac{\partial \dot\Gamma_1}{\partial \tilde x} + (3\alpha - 4)\frac{\partial h_1}{\partial \tilde x}\right) = h_1 - \dot\Gamma_1 - \frac{1 - A}{B} f_1 - \frac{1}{\tan\theta}\frac{\partial h_1}{\partial \tilde x}, \tag{B8}$$

$$\frac{\partial f_1}{\partial \tilde t} = -\frac{1}{\gamma_0^\star}\left(A f_1 - B\dot\Gamma_1\right), \tag{B9}$$

with

$$A \equiv \left(\frac{\mathrm{d}\tilde{\dot\gamma}}{\mathrm{d}\tilde\tau_b}\right)_0 = 1 + \left(\frac{\partial \tilde{\dot\Gamma}}{\partial f_b}\right)_0 B \quad \text{and} \quad B \equiv \left(\frac{\mathrm{d}f_{eq}}{\mathrm{d}\tilde\tau}\right)_0. \tag{B10a,b}$$

The system has non-trivial solutions of the form $h_1 = H\,\mathrm{e}^{\mathrm{i}(\tilde k\tilde x - \tilde\omega\tilde t)}$, $\Gamma_1 = \Gamma\,\mathrm{e}^{\mathrm{i}(\tilde k\tilde x - \tilde\omega\tilde t)}$ and $f_1 = F\,\mathrm{e}^{\mathrm{i}(\tilde k\tilde x - \tilde\omega\tilde t)}$, with $\tilde k$ real and $\tilde\omega$ complex, only if

$$\det\begin{pmatrix} 2\mathrm{i}\tilde k - \mathrm{i}\tilde\omega & \mathrm{i}\tilde k & 0 \\ \dfrac{Re}{3}(3\alpha - 4)\mathrm{i}\tilde k - 1 + \dfrac{\mathrm{i}\tilde k}{\tan\theta} & \dfrac{Re}{3}\left(-\mathrm{i}\tilde\omega + 2(\alpha - 1)\mathrm{i}\tilde k\right) + 1 & \dfrac{1 - A}{B} \\ 0 & -\dfrac{B}{\gamma_0^\star} & -\mathrm{i}\tilde\omega + \dfrac{A}{\gamma_0^\star} \end{pmatrix} = 0, \tag{B11}$$

i.e.

$$-\mathrm{i}\,\frac{Re}{3}\,\tilde{\omega}^3+\left(1+\frac{Re}{3}\,\frac{A}{\gamma_0^\star}+\frac{2\,Re}{3}\,\alpha\mathrm{i}\tilde{k}\right)\tilde{\omega}^2$$
$$+\left(\frac{\mathrm{i}}{\gamma_0^\star}-3\tilde{k}-\frac{2\,Re}{3}\,\frac{A}{\gamma_0^\star}\,\alpha\tilde{k}-\left(\frac{Re}{3}\,\alpha-\frac{1}{\tan\theta}\right)\mathrm{i}\tilde{k}^2\right)\tilde{\omega}$$
$$-\frac{\mathrm{i}}{\gamma_0^\star}\,(2+A)\tilde{k}+\frac{A}{\gamma_0^\star}\left(\frac{Re}{3}\,\alpha-\frac{1}{\tan\theta}\right)\tilde{k}^2=0. \tag{B12}$$

The relation dispersion (B12) has three solutions, which are solved numerically to obtain the behaviour of the branches for arbitrary values of $\tilde{k}$. The long wave asymptotics can also be obtained analytically. At order $O(\tilde{k}^2)$, the first mode is

$$\tilde{\omega}_1=(2+A)\tilde{k}+\mathrm{i}\left[\frac{A}{\tan\theta}\left(\frac{Re}{Re_{Kap}}-1\right)+\gamma_0^\star\left(A^2+A-2\right)\right]\tilde{k}^2, \tag{B13}$$

where Re_{Kap} is the Kapitza threshold without delay depending on A, α and θ (see (3.26)). This is the kinematic mode, with wave speed $\tilde{c}=\mathrm{Re}(\tilde{\omega}_1)/\tilde{k}=2+A$ that is unchanged by the addition of the delay. However, the stability threshold given by $\mathrm{Im}(\tilde{\omega}_1)=0$ is modified by the delay.

We consider, first, the case without inertia ($Re=0$). Equation (B13) shows that the kinematic mode is unstable for $A<A_-$ and for $A>A_+$, where

$$A_\mp=\frac{1-\gamma_0^\star\tan\theta\mp\sqrt{(1-\gamma_0^\star\tan\theta)^2+8\gamma_0^{\star 2}\tan^2\theta}}{2\gamma_0^\star\tan\theta} \tag{B14}$$

are the roots of the polynomial $-A+\gamma_0^\star\tan\theta(A^2+A-2)$. In practice, $\gamma_0^\star\tan\theta\ll 1$, such that $A_-\simeq-2\gamma_0^\star\tan\theta$ and $A_+\simeq 1/2\gamma_0^\star\tan\theta$. Therefore, the delay tends to slightly stabilize the kinematic mode in the case $A<0$ (S-shape flow rule), whereas it destabilizes the flow for $A\gg 1$ (highly shear-thinning fluid). Since $\gamma_0^\star=\gamma_0\,\mathcal{G}(\tau_{b,0})/3$ and $\mathcal{G}(\tau_{b,0})\simeq 3/2$ for $A\simeq 0$ (see (3.20)), we have $\gamma_0^\star\simeq\gamma_0/2$ close to the A_- threshold. Therefore, for a rheology with a small strain delay and in the absence of inertia, the kinematic mode is unstable for

$$A<A_-\simeq-\gamma_0\tan\theta, \tag{B15}$$

where the wave velocity $\tilde{c}_{kin}=2+A_-\simeq 2-\gamma_0\tan\theta$ is slightly below the value 2 obtained when there is no delay (see figure 9*d*).

For a finite inertia ($Re>0$), the stability threshold of the kinematic mode is set by the modified Kapitza Reynolds number

$$Re_{Kap}^{\gamma_0}=Re_{Kap}\left(1+\frac{\gamma_0^\star\tan\theta}{A}\,(2-A-A^2)\right), \tag{B16}$$

and the growth rate can be rewritten as

$$\mathrm{Im}(\tilde{\omega}_1)=\frac{1}{\tan\theta}\left(\frac{Re}{Re_{Kap}^{\gamma_0}}-1\right)(A+\gamma_0^\star\tan\theta\,(2-A-A^2))\tilde{k}^2. \tag{B17}$$

The stability of the kinematic branch depends on the sign of $(Re/Re_{Kap}^{\gamma_0})-1$ and the sign of the polynomial in A. For $A>A_+$, the branch is always unstable. This situation

corresponds to a strongly shear-thinning fluid, not considered here. For $0 < A < A_+$, the mode is unstable for $Re > Re_{Kap}^{\gamma_0}$, which corresponds to the inertial Kapitza waves modified by the presence of a delay. For $A < A_-$ (negatively sloped flow rule), the mode is unstable for low Reynolds numbers $Re < Re_{Kap}^{\gamma_0}$, which corresponds to Oobleck waves. Finally, a small gap exists, $A_- < A < 0$, where the kinematic mode $\tilde{\omega}_1$ is always stable.

The second and third solutions of (B12) at the lowest order in $\tilde{k}$ are

$$\tilde{\omega}_{2,3} = \frac{-\mathrm{i}\left(1 + \dfrac{Re\,A}{3\gamma_0^\star}\right) \mp \mathrm{i}\sqrt{\Delta}}{2\,Re/3}, \tag{B18}$$

with $\Delta = (1 + Re\,A/3\gamma_0^\star)^2 - 4\,Re/3\gamma_0^\star$. They correspond to the inertial branch, which has split in two.

For $\Delta < 0$, the two inertial branches are unstable ($\mathrm{Im}(\tilde{\omega}_{2,3}) > 0$) when $1 + Re\,A/3\gamma_0^\star < 0$. For $A > 0$, this condition is never fulfilled, and the two inertial branches are always stable. However, for $A < 0$, the onset of instability is given by

$$A < A_c = -\frac{3\gamma_0^\star}{Re} \simeq -\frac{3\gamma_0}{2\,Re}, \tag{B19}$$

using as previously $\gamma_0^\star \simeq \gamma_0/2$ for small A. In this case, the frequency of the wave at the onset in the long wave limit is $\mathrm{Re}(\tilde{\omega}_{2,3}) = \pm\sqrt{3/(Re\,\gamma_0^\star)} \simeq \pm\sqrt{6/(Re\,\gamma_0)} \simeq \pm(2/\gamma_0)\sqrt{-A_c}$. The wave velocity $\tilde{c} = \mathrm{Re}(\tilde{\omega}_{2,3})/\tilde{k}$ thus diverges in $\tilde{k} \to 0$.

When $\Delta > 0$, the frequencies $\tilde{\omega}_{2,3}$ are purely imaginary. The imaginary parts are positive (the flow is unstable) if $1 + Re\,A/3\gamma_0^\star < 0$, which is the same condition as (B19). However, in practice, the condition $\Delta > 0$ is reached after that given by (5.3), and the onset of instability is ruled by (5.3) (for $A < 0$).

References

Abdesselam, Y., Agassant, J.-F., Castellani, R., Valette, R., Demay, Y., Gourdin, D. & Peres, R. 2017 Rheology of plastisol formulations for coating applications. *Polym. Engng Sci.* **57** (9), 982–988.

Allouche, M.H., Botton, V., Millet, S., Henry, D., Dagois-Bohy, S., Güzel, B. & Hadid, H.B. 2017 Primary instability of a shear-thinning film flow down an incline: experimental study. *J. Fluid Mech.* **821**, R1.

Balmforth, N.J., Bush, J.W.M. & Craster, R.V. 2005 Roll waves on flowing cornstarch suspensions. *Phys. Lett.* A **338** (6), 479–484.

Balmforth, N.J. & Liu, J.J. 2004 Roll waves in mud. *J. Fluid Mech.* **519**, 33–54.

Benjamin, T.B. 1957 Wave formation in laminar flow down an inclined plane. *J. Fluid Mech.* **2** (6), 554–573.

Blanco, E., Hodgson, D.J.M., Hermes, M., Besseling, R., Hunter, G.L., Chaikin, P.M., Cates, M.E., Van Damme, I. & Poon, W.C.K. 2019 Conching chocolate is a prototypical transition from frictionally jammed solid to flowable suspension with maximal solid content. *Proc. Natl Acad. Sci.* **116** (21), 10303–10308.

Boersma, W.H., Baets, P.J.M., Lavèn, J. & Stein, H.N.J. 1991 Time-dependent behavior and wall slip in concentrated shear thickening dispersions. *J. Rheol.* **35** (6), 1093–1120.

Bonnoit, C., Darnige, T., Clement, E. & Lindner, A. 2010 Inclined plane rheometry of a dense granular suspension. *J. Rheol.* **54** (1), 65–79.

Carpen, I.C. & Brady, J.F. 2002 Gravitational instability in suspension flow. *J. Fluid Mech.* **472**, 201–210.

Chacko, R.N., Mari, R., Cates, M.E. & Fielding, S.M. 2018 Dynamic vorticity banding in discontinuously shear thickening suspensions. *Phys. Rev. Lett.* **121** (10), 108003.

Clavaud, C., Bérut, A., Metzger, B. & Forterre, Y. 2017 Revealing the frictional transition in shear-thickening suspensions. *Proc. Natl Acad. Sci.* **114** (20), 5147–5152.

CLAVAUD, C., METZGER, B. & FORTERRE, Y. 2020 The Darcytron: a pressure-imposed device to probe the frictional transition in shear-thickening suspensions. *J. Rheol.* **64**, 395–403.

COMTET, J., CHATTÉ, G., NIGUÈS, A., BOCQUET, L., SIRIA, A. & COLIN, A. 2017 Pairwise frictional profile between particles determines discontinuous shear thickening transition in non-colloidal suspensions. *Nat. Commun.* **8**, 15633.

DARBOIS TEXIER, B., LHUISSIER, H., FORTERRE, Y. & METZGER, B. 2020 Surface-wave instability without inertia in shear-thickening suspensions. *Commun. Phys.* **3**, 232.

DHAS, D.J. & ROY, A. 2022 Stability of gravity-driven particle-laden flows – roles of shear-induced migration and normal stresses. *J. Fluid Mech.* **938**, A29.

DIVOUX, T., FARDIN, M.A., MANNEVILLE, S. & LEROUGE, S. 2016 Shear banding of complex fluids. *Annu. Rev. Fluid Mech.* **48**, 81–103.

DONG, J. & TRULSSON, M. 2017 Analog of discontinuous shear thickening flows under confining pressure. *Phys. Rev. Fluids* **2** (8), 081301.

FORTERRE, Y. 2006 Kapiza waves as a test for three-dimensional granular flow rheology. *J. Fluid Mech.* **563**, 123–132.

FORTERRE, Y. & POULIQUEN, O. 2003 Long-surface-wave instability in dense granular flows. *J. Fluid Mech.* **486**, 21–50.

FREUNDLICH, H. & RÖDER, H.L. 1938 Dilatancy and its relation to thixotropy. *Trans. Faraday Soc.* **34**, 308–316.

GAUTHIER, A., PRUVOST, M., GAMACHE, O. & COLIN, A. 2021 A new pressure sensor array for normal stress measurement in complex fluids. *J. Rheol.* **65** (4), 583–594.

GODDARD, J.D. 2003 Material instability in complex fluids. *Annu. Rev. Fluid Mech.* **35** (1), 113–133.

GUAZZELLI, É. & POULIQUEN, O. 2018 Rheology of dense granular suspensions. *J. Fluid Mech.* **852**, P1.

GUY, B.M., HERMES, M. & POON, W.C.K. 2015 Towards a unified description of the rheology of hard-particle suspensions. *Phys. Rev. Lett.* **115** (8), 088304.

GUY, B.M., NESS, C., HERMES, M., SAWIAK, L.J., SUN, J. & POON, W.C.K. 2020 Testing the Wyart–Cates model for non-Brownian shear thickening using bidisperse suspensions. *Soft Matt.* **16** (1), 229–237.

HAN, E., WYART, M., PETERS, I.R. & JAEGER, H.M. 2018 Shear fronts in shear-thickening suspensions. *Phys. Rev. Fluids* **3** (7), 073301.

HERMES, M., GUY, B.M., POON, W.C.K., POY, G., CATES, M.E. & WYART, M. 2016 Unsteady flow and particle migration in dense, non-Brownian suspensions. *J. Rheol.* **60** (5), 905–916.

HSU, C.-P., RAMAKRISHNA, S.N., ZANINI, M., SPENCER, N.D. & ISA, L. 2018 Roughness-dependent tribology effects on discontinuous shear thickening. *Proc. Natl Acad. Sci.* **115** (20), 5117–5122.

HWANG, C.-C., CHEN, J.-L., WANG, J.-S. & LIN, J.-S. 1994 Linear stability of power law liquid film flows down an inclined plane. *J. Phys.* D*: Appl. Phys.* **27** (11), 2297–2301.

JEFFREYS, H. 1925 The flow of water in an inclined channel of rectangular section. *Phil. Mag.* **49** (293), 793–807.

VON KANN, S., SNOEIJER, J.H., LOHSE, D. & VAN DER MEER, D. 2011 Nonmonotonic settling of a sphere in a cornstarch suspension. *Phys. Rev.* E **84** (6), 060401.

VON KANN, S., SNOEIJER, J.H. & VAN DER MEER, D. 2013 Velocity oscillations and stop–go cycles: the trajectory of an object settling in a cornstarch suspension. *Phys. Rev.* E **87** (4), 042301.

KAPITZA, P.L. & KAPITZA, S.P. 1948 Wave flow of thin viscous fluid layers. *Zh. Eksp. Teor. Fiz.* **18** (1), 3–28.

LAFARGE 2013 Superplasticizers: the wonder of fluid concrete. https://www.youtube.com/watch?v=CSZxjQwDKF0 **38**.

LANDAU, L.D. & LIFSHITZ, E.M. 2013 *Fluid Mechanics: Landau and Lifshitz: Course of Theoretical Physics*, vol. 6. Elsevier.

LIN, N.Y.C., GUY, B.M., HERMES, M., NESS, C., SUN, J., POON, W.C.K. & COHEN, I. 2015 Hydrodynamic and contact contributions to continuous shear thickening in colloidal suspensions. *Phys. Rev. Lett.* **115** (22), 228304.

LIU, K. & MEI, C.C. 1994 Roll waves on a layer of a muddy fluid flowing down a gentle slope – a Bingham model. *Phys. Fluids* **6** (8), 2577–2590.

LOOTENS, D., VAN DAMME, H. & HÉBRAUD, P. 2003 Giant stress fluctuations at the jamming transition. *Phys. Rev. Lett.* **90** (17), 178301.

MARI, R., SETO, R., MORRIS, J.F. & DENN, M.M. 2014 Shear thickening, frictionless and frictional rheologies in non-Brownian suspensions. *J. Rheol.* **58** (6), 1693–1724.

MARI, R., SETO, R., MORRIS, J.F. & DENN, M.M. 2015*a* Discontinuous shear thickening in Brownian suspensions by dynamic simulation. *Proc. Natl Acad. Sci.* **112** (50), 15326–15330.

MARI, R., SETO, R., MORRIS, J.F. & DENN, M.M. 2015*b* Nonmonotonic flow curves of shear thickening suspensions. *Phys. Rev.* E **91** (5), 052302.
MORRIS, J.F. 2018 Lubricated-to-frictional shear thickening scenario in dense suspensions. *Phys. Rev. Fluids* **3** (11), 110508.
NAGAHIRO, S.-I., NAKANISHI, H. & MITARAI, N. 2013 Experimental observation of shear thickening oscillation. *Europhys. Lett.* **104** (2), 28002.
NAKANISHI, H. & MITARAI, N. 2011 Shear thickening oscillation in a dilatant fluid. *J. Phys. Soc. Japan* **80** (3), 033801.
NG, C.-O. & MEI, C.C. 1994 Roll waves on a shallow layer of mud modelled as a power-law fluid. *J. Fluid Mech.* **263**, 151–184.
OLMSTED, P.D. 1999 Two-state shear diagrams for complex fluids in shear flow. *Europhys. Lett.* **48** (3), 339–345.
OLMSTED, P.D. 2008 Perspectives on shear banding in complex fluids. *Rheol. Acta* **47** (3), 283–300.
OVARLEZ, G., LE, A.V.N., SMIT, W.J., FALL, A., MARI, R., CHATTÉ, G. & COLIN, A. 2020 Density waves in shear-thickening suspensions. *Sci. Adv.* **6** (16), eaay5589.
RAMASWAMY, M., GRINIASTY, I., LIARTE, D.B., SHETTY, A., KATIFORI, E., DEL GADO, E., SETHNA, J.P., CHAKRABORTY, B. & COHEN, I. 2021 Universal scaling of shear thickening transitions. arXiv:2107.13338v2.
RATHEE, V., BLAIR, D.L. & URBACH, J.S. 2017 Localized stress fluctuations drive shear thickening in dense suspensions. *Proc. Natl Acad. Sci.* **114** (33), 8740–8745.
RICHARDS, J.A., ROYER, J.R., LIEBCHEN, B., GUY, B.M. & POON, W.C.K. 2019 Competing timescales lead to oscillations in shear-thickening suspensions. *Phys. Rev. Lett.* **123** (3), 038004.
SAINT-MICHEL, B., GIBAUD, T. & MANNEVILLE, S. 2018 Uncovering instabilities in the spatiotemporal dynamics of a shear-thickening cornstarch suspension. *Phys. Rev.* X **8** (3), 031006.
SEDES, O., SINGH, A. & MORRIS, J.F. 2020 Fluctuations at the onset of discontinuous shear thickening in a suspension. *J. Rheol.* **64** (2), 309–319.
SETO, R., MARI, R., MORRIS, J.F. & DENN, M.M. 2013 Discontinuous shear thickening of frictional hard-sphere suspensions. *Phys. Rev. Lett.* **111** (21), 218301.
SINGH, A., MARI, R., DENN, M.M. & MORRIS, J.F. 2018 A constitutive model for simple shear of dense frictional suspensions. *J. Rheol.* **62** (2), 457–468.
SPENLEY, N.A., YUAN, X.F. & CATES, M.E. 1996 Nonmonotonic constitutive laws and the formation of shear-banded flows. *J. Phys.* II **6** (4), 551–571.
TROWBRIDGE, J.H. 1987 Instability of concentrated free surface flows. *J. Geophys. Res.: Oceans* **92** (C9), 9523–9530.
WHITHAM, G.B. 2011 *Linear and Nonlinear Waves*, vol. 42. John Wiley & Sons.
WYART, M. & CATES, M.E. 2014 Discontinuous shear thickening without inertia in dense non-Brownian suspensions. *Phys. Rev. Lett.* **112** (9), 098302.
YERUSHALMI, J., KATZ, S. & SHINNAR, R. 1970 The stability of steady shear flows of some viscoelastic fluids. *Chem. Engng Sci.* **25** (12), 1891–1902.
YIH, C.-S. 1963 Stability of liquid flow down an inclined plane. *Phys. Fluids* **6** (3), 321–334.
ZAREI, M. & AALAIE, J. 2020 Application of shear thickening fluids in material development. *J. Mater. Res. Technol.* **9** (5), 10411–10433.